

Centrality dependence of particle production in p -Pb collisions at $\sqrt{s_{NN}} = 5.02$ TeV

J. Adam *et al.*^{*}

(ALICE Collaboration)

(Received 15 January 2015; published 8 June 2015)

We report measurements of the primary charged-particle pseudorapidity density and transverse momentum distributions in p -Pb collisions at $\sqrt{s_{NN}} = 5.02$ TeV and investigate their correlation with experimental observables sensitive to the centrality of the collision. Centrality classes are defined by using different event-activity estimators, i.e., charged-particle multiplicities measured in three different pseudorapidity regions as well as the energy measured at beam rapidity (zero degree). The procedures to determine the centrality, quantified by the number of participants (N_{part}) or the number of nucleon-nucleon binary collisions (N_{coll}) are described. We show that, in contrast to Pb-Pb collisions, in p -Pb collisions large multiplicity fluctuations together with the small range of participants available generate a dynamical bias in centrality classes based on particle multiplicity. We propose to use the zero-degree energy, which we expect not to introduce a dynamical bias, as an alternative event-centrality estimator. Based on zero-degree energy-centrality classes, the N_{part} dependence of particle production is studied. Under the assumption that the multiplicity measured in the Pb-going rapidity region scales with the number of Pb participants, an approximate independence of the multiplicity per participating nucleon measured at mid-rapidity of the number of participating nucleons is observed. Furthermore, at high- p_{T} the p -Pb spectra are found to be consistent with the pp spectra scaled by N_{coll} for all centrality classes. Our results represent valuable input for the study of the event-activity dependence of hard probes in p -Pb collisions and, hence, help to establish baselines for the interpretation of the Pb-Pb data.

DOI: 10.1103/PhysRevC.91.064905

PACS number(s): 25.75.Dw, 24.10.Nz, 25.75.Ag

I. INTRODUCTION

Proton-lead collisions are an essential component of the heavy ion program at the Large Hadron Collider (LHC) [1]. Measurements of benchmark processes in p -Pb collisions serve as an important baseline for the understanding and the interpretation of the nucleus-nucleus data. These measurements allow one to disentangle hot-nuclear-matter effects which are characteristic of the formation of the quark-gluon plasma (QGP) from cold-nuclear-matter effects. The latter are the effects due to the presence of the nuclei themselves and not the QGP; for example, k_{T} broadening, nuclear modification of parton densities, and partonic energy loss in cold nuclear matter.

Of particular interest are studies of nuclear effects on parton scatterings at large momentum transfer (hard processes). To this end, we measure the nuclear modification factor, which is defined as the ratio of particle or jet transverse-momentum (p_{T}) spectra in minimum-bias (MB) p -Pb to those in pp collisions scaled by the average number of binary p -nucleon (p -N) collisions ($\langle N_{\text{coll}} \rangle$) [2]. The latter is given by the ratio of p -N and p -Pb inelastic cross sections times the mass number A. In the absence of nuclear effects, the nuclear modification factor is expected to be unity. In heavy-ion collisions, binary scaling is found to hold in measurements of prompt photons [3] and electroweak probes [4,5], which do not

strongly interact with the medium. The observation of binary scaling in p -Pb demonstrates that the strong suppression of hadrons [6], jets [7], and heavy flavor hadrons [8,9] seen in Pb-Pb collisions is due to strong final-state effects. Centrality-dependent measurements of the nuclear modification factor $R_{p\text{Pb}}(p_{\text{T}}, \text{cent})$, defined as

$$R_{p\text{Pb}}(p_{\text{T}}, \text{cent}) = \frac{dN_{\text{cent}}^{p\text{Pb}}/dp_{\text{T}}}{\langle N_{\text{coll}}^{\text{cent}} \rangle dN^{pp}/dp_{\text{T}}}, \quad (1)$$

require the determination of the average $N_{\text{coll}}^{\text{cent}}$ for each centrality class.

Moreover, it has been recognized that the study of p -Pb collisions is also interesting in its own right. Several measurements [10–13] of particle production in the low- and intermediate-transverse-momentum region clearly show that p -Pb collisions cannot be explained by an incoherent superposition of pp collisions. Instead, the data are compatible with the presence of coherent [14] and collective [15] effects. Their strength increases with multiplicity, indicating a strong collision-geometry dependence. In order to corroborate this hypothesis a more detailed characterization of the collision geometry is needed.

The Glauber model [16] is generally used to calculate geometrical quantities of nuclear collisions (A-A or p -A). In this model, the impact parameter b controls the average number of participating nucleons (hereafter referred as “participants” or also “wounded nucleons” [17,18]), N_{part} and the corresponding number of collisions, N_{coll} . It is expected that variations of the amount of matter overlapping in the collision region will change the number of produced particles, and parameters such as N_{part} and N_{coll} have traditionally been used to describe those changes quantitatively and to relate them to pp collisions.

*Full author list given at the end of the article.

By using the Glauber model one can calculate the probability distributions $\pi_\nu(\nu)$, where ν stands for N_{part} or N_{coll} . Since ν cannot be measured directly it has to be related via a model to an observable M , generally called centrality estimator, via the conditional probability $\mathcal{P}(M|\nu)$ to observe M for a given ν . For each collision system and center-of-mass energy, the model has to be experimentally validated by comparing the measured probability distribution $\mathcal{P}_{\text{meas}}(M)$ to the one calculated from the convolution $\mathcal{P}_{\text{calc}}(M) = \sum_\nu \mathcal{P}(M|\nu)\pi_\nu(\nu)$. Once the model has been validated, for each event class defined by an M -interval, the average ν is calculated. In order to unambiguously determine ν , one chooses observables whose mean values depend monotonically on ν . Note that, in p -A collisions, the impact parameter is only loosely correlated to ν . Hence, although one uses traditionally the term centrality to refer to these measurements, the relevant parameters are N_{part} and N_{coll} .

The procedure described above can be easily extended to several estimators. Of particular interest are estimators from kinematic regions that are causally disconnected after the collision. The measurement of a finite correlation between them unambiguously establishes their connection to the common collision geometry. Typically these studies are performed with observables from well-separated pseudorapidity (η) intervals, e.g., at zero degree (spectators, slow nucleons, deuteron breakup probability) and multiplicity in the rapidity plateau.

The use of centrality estimators in p -A collisions based on multiplicity or summed energy in certain pseudorapidity intervals is motivated by the observation that they show a linear dependence on N_{part} or N_{coll} . This is also in agreement with models for the centrality dependence of particle production (e.g., the wounded nucleon model [17,18]), or also string models like FRITIOF [19]). The total rapidity integrated multiplicity of charged particles measured in hadron-nucleus collisions ($N_{\text{ch}}^{\text{h-A}}$) at center-of-mass energies ranging from 10 to 200 GeV (E178 [20], PHOBOS [21]) is consistent with a linear dependence on N_{part} : $N_{\text{ch}}^{\text{h-A}} = N_{\text{ch}}^{\text{pp}} N_{\text{part}}/2$. The ratio of particle pseudorapidity (η) densities in d -Au and pp collisions exhibits a dependence on η , which implies that the scaling behavior has a strong rapidity dependence with an approximate N_{part} scaling at $\eta = 0$ and an approximate scaling with the number of target participants ($N_{\text{part}}^{\text{target}} = N_{\text{part}} - 1$) in the Au-going direction [21]. In d -Au collisions at the BNL Relativistic Heavy Ion Collider (RHIC; $\sqrt{s_{NN}} = 200$ GeV), the PHENIX and STAR collaborations [22,23] have used the multiplicity measured in an η interval of width 0.9 centered at $\eta \approx -3.5$ (Au-going direction) as a centrality estimator. The multiplicity distribution has been successfully described by the Glauber model by assuming $N_{\text{part}}^{\text{target}}$ scaling. Finally, in centrality-averaged p -Pb collisions at the LHC ($\sqrt{s_{NN}} = 5.02$ TeV) the primary charged-particle pseudorapidity density at $\eta = 0$ scaled by the mean number of participants is found to be consistent with the corresponding value in pp collisions interpolated to the same $\sqrt{s_{NN}}$ [24].

At RHIC, the deuteron dissociation probability can be accurately modelled by a Glauber calculation and measured by using the zero-degree calorimeters in the d direction [22,25].

The mean number of participants has been determined for centrality classes obtained with the multiplicity estimator described above and used to calculate the deuteron breakup probability. Inferred and measured probabilities are consistent, demonstrating the correlation between collision geometry and multiplicity and providing a stringent test for the N_{part} determination.

Since, for example, hard scatterings can significantly contribute to the overall particle multiplicity, correlations between high- p_T particle production and bulk multiplicity can also be induced after the collisions and, hence, they are not only related to the collision geometry. Therefore, the use of N_{coll} from the Glauber model to scale cross sections of hard processes from pp to p -A has to undergo the same scrutiny as the correlation of the centrality estimator to the collision geometry. This is necessary also due to the enhanced role of multiplicity fluctuations in p -A. While the average of centrality estimators vary monotonically with ν , for a full description of the conditional probability $\mathcal{P}(M|\nu)$ fluctuations of M for a fixed ν have to be taken into account. In Pb-Pb collisions, these multiplicity fluctuations have little influence on the centrality determination. The range of ν is large and $\mathcal{P}(M|\nu)$ converges with increasing ν rapidly to a Gaussian with small width relative to the range of ν . However, in p -Pb collisions, the range of multiplicities used to select a centrality class is of similar magnitude as the fluctuations, with the consequence that a centrality selection based on multiplicity may select a biased sample of nucleon-nucleon collisions (for a discussion of this effect in d + Au; see Ref. [22]).

In essence, by selecting high (low) multiplicity one chooses not only large (small) average N_{part} , but also positive (negative) multiplicity fluctuations leading to deviations from the binary scaling of hard processes. These fluctuations are partly related to qualitatively different types of collisions. High-multiplicity nucleon-nucleon collisions show a significantly higher particle mean transverse momentum. They can be understood as “harder” collisions, i.e., with higher four-momentum transfer squared Q^2 or as nucleon-nucleon collisions where multiple parton-parton interactions (MPIs) take place.

In contrast, a centrality selection that is not expected to induce a bias on the binary scaling of hard processes is provided by the energy measurement with the zero-degree calorimeters (ZDCs) due to their large η separation from the central barrel detectors. They detect the so-called “slow” nucleons produced in the interaction by nuclear deexcitation processes, or knocked out by wounded nucleons [26,27]. The relationship of the energy deposited in the ZDC to the number of collisions requires a detailed model to describe the slow nucleon production. A heuristic approach, based on a parametrization of data from low-energy experiments, is discussed in the present paper.

We show that centrality estimators using forward neutron energy and those using central multiplicity give consistent results for N_{part} and N_{coll} , demonstrating their connection to the collision geometry. Based on the considerations outlined above we study two different procedures for centrality estimation. The first procedure is to determine the centrality with charged-particle multiplicity. The collision geometry is determined by fitting the measured multiplicity distribution with the

N_{coll} distribution obtained from the Glauber model [16], convolved with a negative binomial distribution (NBD). Due to the possible dynamical bias introduced by the multiplicity selection, N_{coll} should in this case not be used to scale hard cross sections. Additional effort is needed to understand the bias or to extend the Glauber model to include additional dynamical fluctuations. Several possible directions have been discussed, for example, Glauber–Gribov fluctuations of the proton size [28] as well as fluctuations of the number of hard scatterings per collision due to the impact-parameter dependence and purely statistical (Poissonian) fluctuations [29].

The second procedure requires a centrality selection with minimal bias and, therefore, uses the ZDC signal. To relate the ZDC signal to the collision geometry we developed a heuristic model for slow-nucleon emission based on a parametrization of data from low-energy experiments. This heuristic approach, however, can provide only a model-dependent N_{coll} determination. However, one can study the correlation of two or more observables out of which at least one is expected to scale linearly with N_{coll} . Examples are (i) the target-going multiplicity proportional to the number of wounded target nucleons ($N_{\text{part}}^{\text{target}} = N_{\text{part}} - 1 = N_{\text{coll}}$), (ii) the multiplicity at midrapidity proportional to the number of participants ($N_{\text{part}} = N_{\text{coll}} + 1$), (iii) the yield of hard probes, like high- p_{T} particles at midrapidity proportional to N_{coll} . These scalings can be used as an ansatz when calculating N_{coll} based on an event selection using the ZDC.

Both alternatives are discussed in the present paper. The paper is organized as follows: Section II describes the experimental conditions, the event selection, and the event characterization using the multiplicity distributions of charged particles measured in various η ranges, or the energy collected in the ZDC. Section III describes the centrality determination based on charged-particle distributions using an NBD-Glauber fit to extract the average geometrical quantities for typical centrality classes. Section IV presents a phenomenological model describing the relation of the energy deposited in the ZDC calorimeter and N_{coll} . Section V discusses the various effects leading to a bias in the centrality measurements based on particle multiplicity. Section VI introduces a hybrid method, where we use the ZDC to characterize the event activity, and base the determination of N_{coll} on the assumption that N_{part} -scaling holds for the central pseudorapidity multiplicity density or $N_{\text{part}}^{\text{target}}$ -scaling for particle production in the target region. Section VII discusses the implications of the different choices of a centrality estimator on the physics results, such as the nuclear modification factors, or the pseudorapidity density of charged particles at midrapidity. Section VIII summarizes and concludes the paper.

II. EXPERIMENTAL CONDITIONS

The data were recorded during a dedicated LHC run of four weeks in January and February, 2013. Data were taken with two beam configurations by inverting the direction of the two particle species, referred to as $p\text{-Pb}$ and $\text{Pb}\text{-}p$, respectively, for the situations where the proton beam is moving towards positive rapidities, or vice versa. The two-in-one-magnet design of the LHC imposes the same magnetic rigidity of the

beams in the two rings, implying that the ratio of beam energies is fixed to be exactly equal to the ratio of the charge/mass ratios of each beam. Protons at 4 TeV energy collided onto fully stripped $^{208}_{82}\text{Pb}$ ions at 1.58 TeV per nucleon energy resulting in collisions at $\sqrt{s_{\text{NN}}} = 5.02$ TeV in the nucleon–nucleon center-of-mass system (cms), which moves with a rapidity of $\Delta y_{\text{NN}} = 0.465$ in the direction of the proton beam. In the following, we use the convention that y stands for y_{cms} , defined such that the proton moves towards positive η_{cms} , while η stands for η_{lab} .

The number of colliding bunches varied from 8 to 288. The proton and Pb bunch intensities were ranging from 0.2×10^{12} to 6.5×10^{12} and from 0.1×10^{12} to 4.4×10^{12} , respectively. The luminosity at the ALICE interaction point was up to $5 \times 10^{27} \text{ cm}^{-2} \text{ s}^{-1}$ resulting in a 10 kHz hadronic interaction rate. The rms width of the interaction region is 6.3 cm along the beam direction and of about 60 μm in the direction transverse to the beam.

The ALICE apparatus and its performance in the LHC Run 1 are described in Refs. [30,31], respectively. The main detector components used for the centrality determination are the Silicon Pixel Detector (SPD), two cylindrical layers of hybrid silicon pixel assemblies covering $|\eta| < 2.0$ for the inner layer and $|\eta| < 1.4$ for the outer layer for vertices at the nominal interaction point, with 93.5% active channels; the Time Projection Chamber (TPC), a large cylindrical drift detector covering $|\eta| < 0.9$; the VZERO scintillator counters, covering the full azimuth within $2.8 < \eta < 5.1$ (VZERO-A) and $-3.7 < \eta < -1.7$ (VZERO-C); and the Zero-Degree Calorimeters (ZDC), two sets of neutron (ZNA and ZNC) and proton (ZPA and ZPC) calorimeters positioned at ± 112.5 m from the interaction point, with an energy resolution of about 20% for the neutron and 24% for the proton calorimeters.

The $p\text{-Pb}$ trigger, configured to have high efficiency for hadronic events, requires a signal in both the VZERO-A and VZERO-C (VZERO-AND requirement). Beam-gas and other machine-induced background collisions with deposited energy above the thresholds in the VZERO or ZDC detectors are suppressed by requiring the signal arrival time to be compatible with a nominal $p\text{-Pb}$ interaction. The fraction of remaining beam-related background after all requirements is estimated from control triggers on noncolliding or empty bunches and is found to be negligible.

The resulting event sample corresponds to a so-called *visible cross section* of 2.09 ± 0.07 barn measured in a van der Meer scan [32]. From Monte Carlo simulations we expect that the sample consists mainly of non-single-diffractive (NSD) collisions and a negligible contribution of single-diffractive (SD) and electromagnetic interactions. The VZERO-AND trigger is not fully efficient for NSD events. Previous Monte Carlo studies (for details see Ref. [24]) have shown that the inefficiency is observed mostly for events without a reconstructed vertex, i.e., with no particles produced at central rapidities. Given the fraction of such events in the data (1.5%), the corresponding inefficiency was found to be 2.2% with a large systematic uncertainty of 3.1%. Correcting for this inefficiency would mainly concern the most peripheral class (80% to 100%) where the correction amounts up to $11\% \pm 15.5\%$. For the results reported in this paper, centrality

classes have been defined as percentiles of the visible cross section and the measurements are not corrected for trigger inefficiency.

The centrality determination is performed by exploiting the rapidity coverage of the various detectors. The raw multiplicity distributions measured in the Central Barrel are modelled by assuming particle production sources are distributed according to a NBD. The zero-degree energy of the slow nucleons emitted in the nucleon fragmentation requires more detailed models.

In this context, the main estimators used for centrality in the following are

- (i) CL1: the number of clusters in the outer layer of the silicon pixel detector, $|\eta| < 1.4$;
- (ii) V0A: the amplitude measured by the VZERO hodoscopes on the A side (the Pb-going side in the p -Pb event sample), $2.8 < \eta < 5.1$;
- (iii) V0C: the amplitude measured by the VZERO hodoscopes on the C side (the p -going side in the p -Pb event sample), $-3.7 < \eta < -1.7$;
- (iv) V0M: the sum of the amplitudes in the VZERO hodoscopes on the A and C side ($V0A + V0C$);
- (v) ZNA: the energy deposited in the neutron calorimeter on the A side (the Pb-going side in the p -Pb event sample).

III. CENTRALITY FROM CHARGED-PARTICLE DISTRIBUTIONS

A. Negative binomial distribution Glauber fit

To determine the relationship between charged-particle multiplicity and the collision properties, such as the number of participating nucleons N_{part} , binary pN collisions N_{coll} , or nuclear overlap $T_{p\text{Pb}}$ ($=N_{\text{coll}}/\sigma_{NN}^{\text{inel}}$), it is customary to use the Glauber Monte Carlo (Glauber MC) model combined with a simple model for particle production [33–37]. The method was used in Pb-Pb collisions and is described in detail in Ref. [38]. In the Glauber calculation, the nuclear density for ^{208}Pb is modelled by a Woods-Saxon distribution for a spherical nucleus

$$\rho(r) = \rho_0 \frac{1}{1 + \exp\left(\frac{r-R}{a}\right)}, \quad (2)$$

with ρ_0 being the nucleon density, which provides the overall normalization, a radius of $R = 6.62 \pm 0.06$ fm, and a skin depth of $a = 0.546 \pm 0.010$ fm based on data from low-energy electron-nucleus scattering experiments [39]. Nuclear collisions are modelled by randomly displacing the projectile proton and the target Pb nucleus in the transverse plane. A hard-sphere exclusion distance of 0.4 fm between nucleons is employed. The proton is assumed to collide with the nucleons of the Pb nucleus if the transverse distance between them is less than the distance corresponding to the inelastic nucleon-nucleon cross section of 70 ± 5 mb at $\sqrt{s} = 5.02$ TeV, estimated from interpolating data at different center-of-mass energies [40] including measurements at 2.76 and 7 TeV [41]. The VZERO-AND cross section measured in a van der Meer scan [32] was found to be compatible, assuming negligible efficiency and electromagnetic contamination corrections,

TABLE I. Fit parameters of the $N_{\text{part}} \times$ NBD for pp collisions at 7 TeV and p -Pb multiplicity distributions.

System distribution	pp		p -Pb	
	μ	k	μ	k
V0A	9.6	0.56	11.0	0.44
V0M	25.2	0.82	23.6	1.08
CL1	9.8	0.64	8.74	0.76

with the Glauber-derived p -nucleus inelastic cross section of 2.1 ± 0.1 b. The Glauber MC determines on an event-by-event basis the properties of the collision geometry, such as N_{part} , N_{coll} , and $T_{p\text{Pb}}$, which must be mapped to an experimental observable.

Assuming that the average V0A multiplicity is proportional to the number of participants in an individual p -A collision, the probability distribution $P(n)$ of the contributions n to the amplitude from each p -nucleon collisions can be described by the NBD, which is defined as

$$P(n; \mu, k) = \frac{\Gamma(n+k)}{\Gamma(n+1)\Gamma(k)} \frac{(\mu/k)^n}{(\mu/k+1)^{n+k}}, \quad (3)$$

where Γ is the gamma function, μ the mean amplitude per participant and the dispersion parameter k is related to the relative width given by $\sigma/\mu = \sqrt{1/\mu + 1/k}$. From the closure of the NBD under convolution, it follows that the conditional probability $P(n|N_{\text{part}})$, i.e., N_{part} repeated convolutions, is equal to $P(n; N_{\text{part}}\mu, N_{\text{part}}k)$.

To obtain the NBD parameters μ and k , the calculated V0A distribution, obtained by convolving the Glauber N_{part} distribution with $P(n|N_{\text{part}})$, is fit to the measured V0A distribution. The fit is performed by excluding the low-V0A-amplitude region, $V0A < 10$. We note, however, that fitting with the full range gives consistent results. The measured V0A distribution together with the NBD-Glauber distribution for the best fit are shown in Fig. 1. Similar fits have been performed

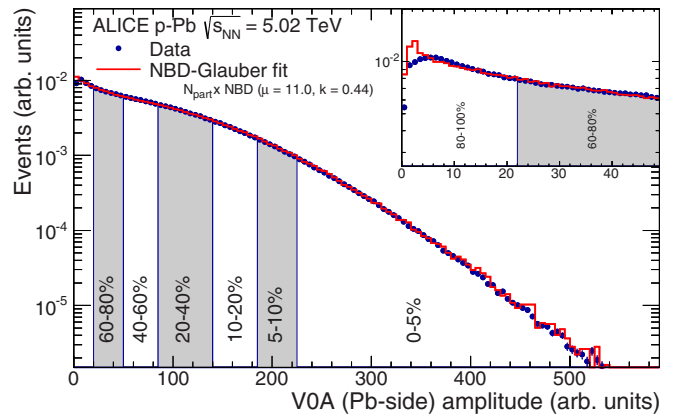


FIG. 1. (Color online) Distribution of the sum of amplitudes in the V0A hodoscopes (Pb-going), as well as the NBD-Glauber fit (explained in the text). Centrality classes are indicated by vertical lines. The inset shows a zoom in on the most peripheral events.

TABLE II. Geometric properties (b , $T_{p\text{Pb}}$, N_{part} , N_{coll}) of p -Pb collisions for centrality classes defined by cuts in V0A. The mean values and the σ values are obtained with a Glauber Monte Carlo calculation, coupled to a NBD to fit the V0A distribution.

Centrality (%)	$\langle b \rangle$ (fm)	σ (fm)	$\langle T_{p\text{Pb}} \rangle$ (mb $^{-1}$)	σ (mb $^{-1}$)	$\langle N_{\text{part}} \rangle$	σ	$\langle N_{\text{coll}} \rangle$	σ
0–5	3.12	1.39	0.211	0.0548	15.7	3.84	14.7	3.84
5–10	3.50	1.48	0.186	0.0539	14.0	3.78	13.0	3.78
10–20	3.85	1.57	0.167	0.0549	12.7	3.85	11.7	3.85
20–40	4.54	1.69	0.134	0.0561	10.4	3.93	9.36	3.93
40–60	5.57	1.69	0.0918	0.0516	7.42	3.61	6.42	3.61
60–80	6.63	1.45	0.0544	0.0385	4.81	2.69	3.81	2.69
80–100	7.51	1.11	0.0277	0.0203	2.94	1.42	1.94	1.42
0–100	5.56	2.07	0.0983	0.0728	7.87	5.10	6.87	5.10

to V0M and CL1 and the corresponding fit parameters are listed in Table I. The values of the parameters μ and k are similar to those obtained by fitting the corresponding multiplicity distributions in pp collisions at 7 TeV. Since the raw distribution is sensitive to experimental parameters such as noise and gain, one cannot expect identical values even in the case of perfect N_{part} scaling and therefore the comparison is only qualitative.

For a given centrality class, defined by selections in the measured distribution, the information from the Glauber MC in the corresponding generated distribution is used to calculate the mean number of participants $\langle N_{\text{part}} \rangle$, the mean number of collisions $\langle N_{\text{coll}} \rangle$, and the average nuclear overlap function $\langle T_{p\text{Pb}} \rangle$. These are given in Table II, with the corresponding σ values. Since the event selection dominantly selects NSD events, it is important to note that the number of participants in the Glauber calculation would increase by only 2.5% for NSD events. This was estimated with a modified Glauber calculation to exclude SD collisions [24].

The systematic uncertainties are evaluated by varying the Glauber parameters (radius, skin depth, and hard-sphere exclusion distance) within their known uncertainty. The uncertainties on $\langle N_{\text{coll}} \rangle$ are listed in Table III by adding all the deviations from the central result in quadrature. The uncertainties range from about 4%–5% in peripheral collisions to about 10% in central collisions. Note that, as $T_{p\text{Pb}} = N_{\text{coll}}/\sigma_{NN}^{\text{inel}}$, the uncertainties on $\sigma_{NN}^{\text{inel}}$ and $\langle N_{\text{coll}} \rangle$ largely cancel in the calculation of $T_{p\text{Pb}}$. However, edge

effects in the nuclear overlap are large for $T_{p\text{Pb}}$ in peripheral collisions.

The procedure was tested with a MC-closure test using HIJING p -Pb simulations [29] with nuclear modifications of the parton density (shadowing) and elastic scattering switched off. In the MC-closure test, the V0A distribution obtained from a detailed detector simulation coupled to HIJING was taken as the input for the fit with the NBD-Glauber method. The difference between the $\langle N_{\text{coll}} \rangle$ values calculated from the fit and those from the MC truth used in the HIJING simulation range from 3% in central to 23% in peripheral events (see Table III). The large uncertainty in the peripheral events arises from the small absolute values of N_{coll} itself. In this case a small absolute uncertainty results in a large relative deviation. The total uncertainty on $\langle N_{\text{coll}} \rangle$ for each centrality class with the CL1, V0M, or V0A estimators is obtained by adding the uncertainty from the variation of the Glauber parameters with those from the respective MC-closure test in quadrature.

The NBD-Glauber fit is repeated for the multiplicity distribution of the SPD clusters (CL1) and for the sum of V0A and V0C, V0M, in the same centrality classes as for V0A. The $\langle N_{\text{coll}} \rangle$ values as a function of centrality are given in Table III and shown in Fig. 2 for the various estimators. In addition, the events from the MC-Glauber calculation were ordered according to their impact parameter, and the values of $\langle N_{\text{coll}} \rangle$ were extracted for the same centrality classes. The variation of N_{coll} between different centrality estimators is small and of similar magnitude as the systematic uncertainty

TABLE III. Comparison of $\langle N_{\text{coll}} \rangle$ values. In the first column results are listed for centrality classes obtained by ordering the events according to the impact parameter distribution (b). In the next three columns $\langle N_{\text{coll}} \rangle$ values are given for the various centrality estimators CL1, V0A, V0M. The systematic uncertainty on $\langle N_{\text{coll}} \rangle$ (in parentheses on $T_{p\text{Pb}}$) is obtained by changing all Glauber parameters by 1σ ; the second column is obtained from the MC-closure test; those two are added in quadrature to obtain the total systematic uncertainty on $\langle N_{\text{coll}} \rangle$. The last column gives the $\langle N_{\text{coll}} \rangle$ values obtained for the ZNA (see Sec. IV) and the uncertainty on the slow nucleon model (SNM, see Sec. IV).

Centrality (%)	$\langle N_{\text{coll}}^b \rangle$	$\langle N_{\text{coll}}^{\text{CL1}} \rangle$	$\langle N_{\text{coll}}^{\text{V0M}} \rangle$	$\langle N_{\text{coll}}^{\text{V0A}} \rangle$	Sys. Glauber	Sys. MC closure	Sys. Total	$\langle N_{\text{coll}}^{\text{ZNA}} \rangle$	Sys. SNM
0–5	14.4	15.6	15.7	14.8	10% (3.7%)	3%	10%	15.7	7%
5–10	13.8	13.6	13.7	13.0	10% (3.5%)	1%	10%	13.9	5%
10–20	12.7	12.0	12.1	11.7	10% (3.2%)	2%	10%	12.4	2%
20–40	10.2	9.49	9.55	9.36	8.8% (3.1%)	2%	9%	9.99	2%
40–60	6.30	6.18	6.26	6.42	6.6% (4.3%)	3%	7.2%	6.53	4%
60–80	3.10	3.40	3.40	3.81	4.3% (6.7%)	20%	20%	3.04	4%
80–100	1.44	1.76	1.72	1.94	2.0% (9.3%)	23%	23%	1.24	8%
0–100	6.88	6.83	6.87	6.87	8% (3.4%)		8%	6.88	

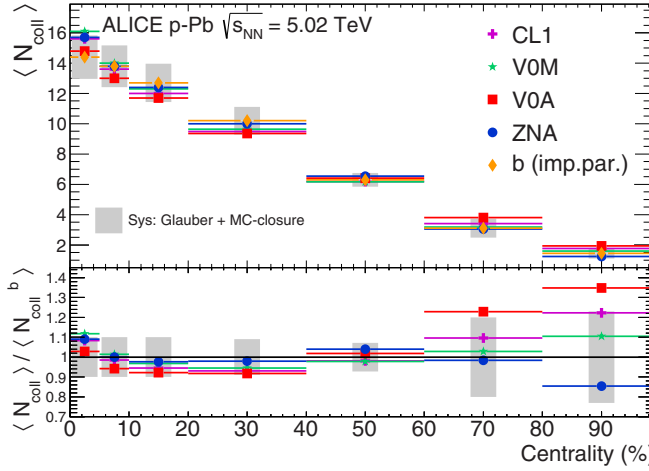


FIG. 2. (Color online) Values of $\langle N_{\text{coll}} \rangle$ extracted from CL1, VOM, VOA, ZNA and by ordering the events according to the impact parameter distribution (b). The systematic uncertainty, given by the quadrature sum of the uncertainty from the Glauber parameters and the MC-closure test, are drawn around the values obtained with b .

obtained by adding in quadrature the uncertainty from the Glauber model and from the MC-closure test. This implies that the $\langle N_{\text{coll}} \rangle$ determination with the NBD-Glauber fit is robust and independent of the centrality estimator used.

B. Glauber–Gribov corrections

Event-by-event fluctuations in the configuration of the incoming proton can change its scattering cross section [28]. In the Glauber MC this phenomenon is implemented by an effective scattering cross section [42–44]. At high energies, the configuration of the proton is taken to be frozen over the timescale of the p -A collision. Analogously to the studies in Refs. [45,46], the effect of these frozen fluctuations of the projectile proton is evaluated with a modified version of the Glauber MC, referred to as “Glauber–Gribov.” This version includes event-by-event variations of the nucleon-nucleon

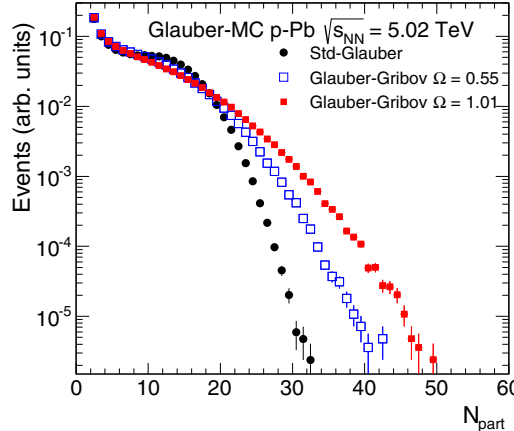


FIG. 3. (Color online) (left) Glauber and Glauber–Gribov Monte Carlo N_{part} distributions for 5.02 TeV $p\text{-Pb}$ collisions. (right) Measured VOA distribution compared to Glauber and Glauber–Gribov fits assuming N_{part} or N_{coll} scaling. The inset shows a zoom in on the most peripheral events.

TABLE IV. Fit parameters of the VOA distributions using standard Glauber and Glauber–Gribov ($\Omega = 0.55$) distributions of N_{part} and N_{coll} coupled to a NBD.

Distribution	μ	k
Std-Glauber and $N_{\text{coll}} \otimes \text{NBD}$	12.2	0.58
Std-Glauber and $N_{\text{part}} \otimes \text{NBD}$	11.0	0.44
Glauber–Gribov and $N_{\text{coll}} \otimes \text{NBD}$	12.6	1.35
Glauber–Gribov and $N_{\text{part}} \otimes \text{NBD}$	11.0	0.60

cross section. Here we have used the same values of the parameter Ω , which controls the width of the probability distribution of $\sigma_{\text{NN}}^{\text{inel}}$, as used in Ref. [45]; namely, $\Omega = 0.55$ and 1.01, where $\Omega = 0.0$ corresponds to the standard Glauber.

The distribution of the number of participants, N_{part} , obtained from the two Glauber–Gribov parameter variations are shown in the left panel of Fig. 3 together with a standard N_{part} distribution obtained using a fixed inelastic cross section, $\sigma_{\text{NN}}^{\text{inel}} = 70 \text{ mb}$. The Glauber–Gribov N_{part} distributions are much broader than the Glauber distribution due to the cross-section fluctuations. We note that by construction the total inelastic $p\text{-Pb}$ cross section is unaltered by the proton fluctuations.

The Glauber–Gribov distributions of N_{part} and N_{coll} , coupled to a NBD, were fit to the measured distribution of VOA. The right panel of Fig. 3 shows the VOA distribution together with various fits performed with the standard Glauber or the Glauber–Gribov distribution, using $\Omega = 0.55$, and assuming that the signal increases proportionally either to N_{part} or to N_{coll} . As before, no attempt is made to describe the most peripheral region (below $\sim 90\%$), where trigger efficiency is not 100%. The extracted parameters are given in Table IV.

The standard NBD-Glauber fits yield satisfactory results using either the N_{part} or the N_{coll} scaling, which result in a similar average number of collisions $\langle N_{\text{coll}} \rangle$, evaluated for each of the centrality intervals as shown in Table V. The Glauber–Gribov fits with $\Omega = 0.55$ provide an equally good description of the measured VOA distribution as the standard Glauber, indicating that the fits cannot discriminate between the models.

TABLE V. N_{coll} values obtained for various fits of the V0A, using Std-Glauber ($\Omega = 0.0$) and Glauber–Gribov ($\Omega = 0.55$) distributions for N_{part} or N_{coll} , coupled to a NBD.

Centrality (%)	Std-Glauber		Glauber-Gribov	
	$N_{\text{part}} \times \text{NBD}$	$N_{\text{coll}} \times \text{NBD}$	$N_{\text{part}} \times \text{NBD}$	$N_{\text{coll}} \times \text{NBD}$
0–5	14.8	15.3	17.8	19.2
5–10	13.0	13.4	14.4	15.2
10–20	11.7	12.0	12.0	12.5
20–40	9.36	9.62	8.82	9.04
40–60	6.42	6.40	5.68	5.56
60–80	3.81	3.42	3.33	2.89
80–100	1.94	1.85	1.72	1.43
0–100	6.87	6.87	6.73	6.75

The broader N_{part} distributions in the Glauber–Gribov models require smaller intrinsic fluctuations in the NBD at fixed N_{part} . No satisfactory fit is obtained with $\Omega = 1.01$. As expected, the corresponding values of $\langle N_{\text{coll}} \rangle$, also shown in Table V, are larger (smaller) for central (peripheral) than those obtained from the standard Glauber, as a consequence of the different shapes of the N_{part} distributions in these models [see Fig. 3 (left)]. Both assumptions that the multiplicity distribution is proportional to N_{part} or N_{coll} are found to give an equally good description of the experimental data (see Fig. 3, and parameters reported in Table IV). The difference in the extracted geometric quantities is within 10% for 0%–60% and slightly increases for the most peripheral, which is of similar order as the uncertainty derived from the Glauber parameters (see the last two columns of Table V).

IV. CENTRALITY FROM ZERO-DEGREE ENERGY

The energy measured in the zero-degree calorimeters (ZDCs) can be used to determine the centrality of the collision. The ZDC detects the so-called “slow” nucleons produced in the interaction: protons in the proton ZDC (ZP) and neutrons in the neutron ZDC (ZN). The multiplicity of slow nucleons

is expected to be monotonically related to N_{coll} [26] and can therefore be used as a centrality estimator.

Emitted nucleons are classified as “black” or “gray.” This terminology originates from emulsion experiments where it was related to the track grain density. Black particles, typically defined to have velocity $\beta \lesssim 0.25$ in the nucleus rest frame, are produced by nuclear evaporation processes, while gray particles, $0.25 \lesssim \beta \lesssim 0.7$, are mainly nucleons knocked out from the nucleus. Experimental results at lower energies show that the features of the emitted nucleons, such as angular-momentum and multiplicity distributions, are weakly dependent on the projectile energy in a wide range from 1 GeV up to 1 TeV (see Ref. [26] and references therein). These observations suggest that the emission of slow particles is mainly dictated by nuclear geometry.

To quantitatively relate the energy deposited in the ZDC to the number of binary collisions requires a model to describe the production of slow nucleons. Since there are no models available that are able to describe the slow nucleon emission at LHC energies, we relied on the weak dependence on collision energy and followed a heuristic approach. For this purpose we developed a model for the slow-nucleon emission (SNM) based on the parametrization of experimental results at lower energies.

In the left panel of Fig. 4 it is shown that the energy detected by the neutron calorimeter on the Pb-remnant side (ZNA) is correlated with the energy detected in the proton ZDC (ZPA), up to the onset of a saturation in the emission of neutrons. This saturation effect is commonly attributed to the black component (see Ref. [26] and references therein). The energy detected by ZP is lower. This is due both to the lower number of protons in the Pb nucleus and to the lower acceptance for emitted protons that are affected by LHC magnetic fields. Furthermore, contrary to ZN, ZP response and energy resolution strongly depend on the proton impact point. In the following we focus on the ZN spectrum for these reasons.

The energy released in the ZNA is anticorrelated with the signal in the neutron calorimeter placed on the p -remnant side (ZNC) (see Fig. 4, right). The p -remnant-side ZN signal

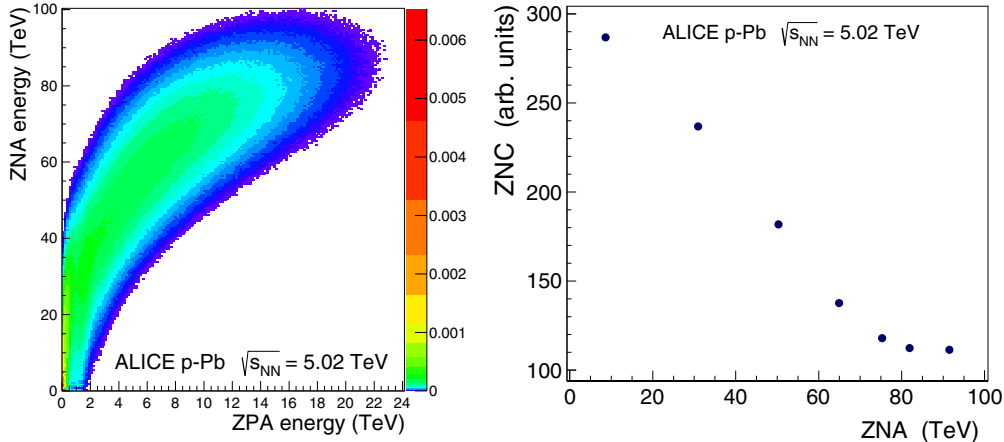


FIG. 4. (Color online) (left) Correlation between Pb remnant neutron (ZNA) and proton (ZPA) calorimeter energies. (right) Average signal on the p remnant side (ZNC) versus average energy detected by ZNA in centrality bins selected using ZNA.

cannot be easily calibrated in energy units due to the lack of peaks in the spectrum. Events characterized by low- N_{coll} values, corresponding to low energy deposit in ZNA, have the largest contribution in ZNC. This implies that the participant contribution cannot be neglected for very peripheral events, where the sample is also partially contaminated by electromagnetic processes. Therefore, supposing that no nucleons are emitted in the limit that there is no collision, the model is not expected to provide a complete and reliable description for very peripheral data.

In the following, we briefly summarize the main ingredients of the developed heuristic model for slow-nucleon emission. The average number of emitted gray protons is calculated as a function of N_{coll} by using a second-order polynomial function:

$$\langle N_{\text{gray } p} \rangle = c_0 + c_1 N_{\text{coll}} + c_2 N_{\text{coll}}^2. \quad (4)$$

This relationship was found to be in good agreement with gray proton data measured by E910 in p -Au collisions with an 18 GeV/c proton beam [47]. The coefficient values taken from the E910 fit are rescaled to Pb nuclei by using the ratio ($Z_{\text{Pb}}/Z_{\text{Au}}$): $c_0 = -0.24$, $c_1 = 0.55$, $c_2 = 0.0007$. The linear term is the dominant contribution while the quadratic term is negligible. Neglecting in this context a possible saturation effect for black protons, we approximate the average number of black protons using the ratio between “evaporated” and “direct” proton production measured by the COSY experiment in p -Au interactions at 2.5 GeV [48]: $\langle N_{\text{black } p} \rangle = 0.65 \langle N_{\text{gray } p} \rangle$.

The average number of slow neutrons is obtained using the following formula:

$$\langle N_{\text{slow } n} \rangle = \alpha N_{\text{LCF}} + \left(a - \frac{b}{c + N_{\text{LCF}}} \right), \quad (5)$$

where N_{LCF} is the number of light charged fragments; namely, the number of fragments with $Z < 8$. Since we cannot directly measure the number of light charged fragments in ALICE, we assumed that N_{LCF} is proportional to the number of slow protons as measured by COSY [48]: $N_{\text{LCF}} = \gamma \langle N_{\text{slow } p} \rangle$ where the proportionality factor $\gamma = 1.71$ is obtained through a minimization procedure. The first term in Eq. (5) describes the gray neutron production that linearly increases with N_{coll} and hence with N_{LCF} . The second term reproduces the saturation in the number of black nucleons and is based on a parametrization of results from the COSY experiment where the neutron yield is related to N_{LCF} [48]. The values of the parameters α , a , b , and c are obtained through a minimization procedure and are $\alpha = 0.48$, $a = 50$, $b = 230$, $c = 4.2$.

The relative fraction of black and gray neutrons is evaluated by assuming that 90% of the emitted neutrons are black, as measured in proton-induced spallation reactions in the energy range between 0.1 and 10 GeV [49]. The number of nucleons emitted from ^{208}Pb is finally calculated event by event as a function of N_{coll} , assuming binomial distributions with probabilities $p = \langle N_{\text{slow } p} \rangle / 82$ for protons and $p = \langle N_{\text{slow } n} \rangle / 126$ for neutrons.

The kinematical distributions of the black and the gray components are described by independent statistical emission from a moving frame: black nucleons are emitted from a stationary source, while gray nucleons are emitted from a frame slowly moving along the beam direction with $\beta_{\text{gray}} = 0.05$.

The angular distribution for gray tracks is forward peaked in the polar angle θ , while black nucleons are assumed to be uniformly distributed, in agreement with the experimental observations [47,50].

The neutron calorimeter has full geometric acceptance for neutrons emitted from the Pb nucleus, as estimated through Monte Carlo simulations. Experimentally, a fraction of triggered events (4.4%) does not produce a signal in ZN, these are very peripheral events with no neutron emission. The convolution of ZN acceptance and efficiency has been calculated coupling an event generator based on the SNM to HIJING [29] and using a full GEANT 3 [51] description of the ALICE experimental apparatus. Taking into account the experimental conditions (beam-crossing angle and detector configuration), we obtain that 94% of the events have a signal in the neutron calorimeter, in good agreement with the experimental acceptance (95.6%). Since the events without ZNA signal have the same CL1, V0A, and V0M distributions as those in the 80%–100% centrality bin, they are attributed to this bin.

The SNM, coupled to the probability distribution for N_{coll} calculated from the Glauber MC as in Sec. III A, is fit to the experimental distribution of the ZDC energy in Fig. 5. The detector acceptance and resolution are fixed to the experimental values. The parameters that are obtained by fitting the data are γ , a , b , c , and α . The main features of the measured energy distribution in the neutron calorimeter on the Pb side are reasonably well described by the SNM. The $\langle N_{\text{coll}} \rangle$, reported in Table III and in Fig. 2, is then

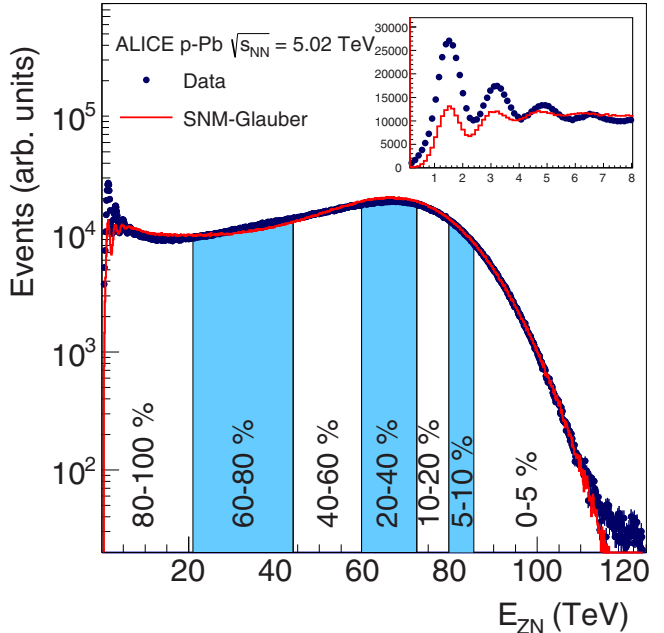


FIG. 5. (Color online) Distribution of the neutron energy spectrum measured in the Pb-remnant-side ZN calorimeter. The distribution is compared with the corresponding distribution from the SNM-Glauber model (explained in the text), which is shown as a line. Centrality classes are indicated in the figure. The inset shows a zoom in on the most peripheral events.

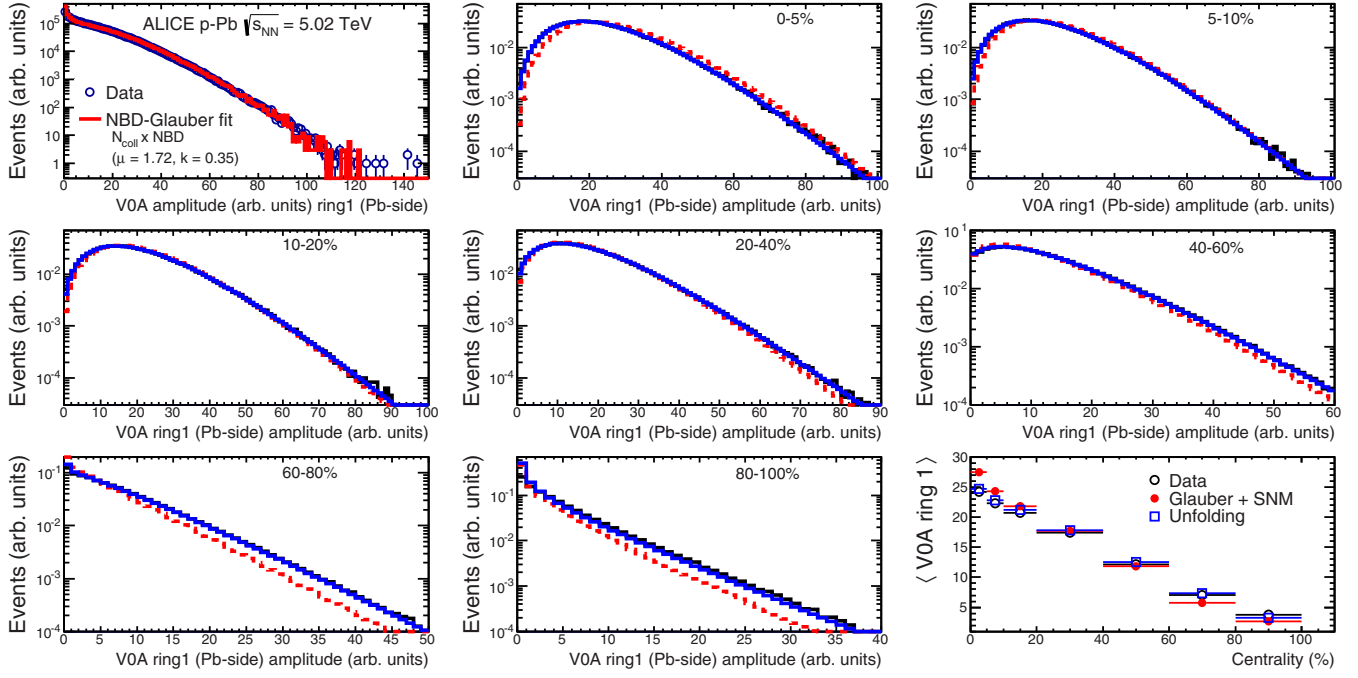


FIG. 6. (Color online) VOA ring 1 signal distributions. The top-left panel shows the distribution for MB events together with a NBD-Glauber fit. The remaining panels show the distributions and mean values for centrality classes selected with ZNA. These are compared to those obtained by the convolution of the $\mathcal{P}(N_{\text{coll}}|\text{cent}_{\text{ZNA}})$ distributions from the SNM with the NBD from the NBD-Glauber fit to VOA ring 1. Data are also compared to the distributions obtained with an unfolding procedure, where the N_{coll} distributions have been fit to the data by using the parameters from the NBD-Glauber fit. The bottom-right panel compares the mean values of these distributions as a function of the centrality.

calculated for centrality classes defined by dividing the energy spectrum in percentiles of the hadronic cross section. The systematic uncertainty on the N_{coll} values reported in Table III, has been evaluated by varying the model parameters within reasonable ranges: (i) using for the relative fraction of black over gray protons $\langle N_{\text{black},p} \rangle = 0.43 \langle N_{\text{gray},p} \rangle$ from spallation reaction results [49], (ii) including a saturation effect for black protons, (iii) decreasing the ratio of black over gray neutrons to 0.5 as obtained from DPMJET [52], (iv) neglecting the linear term in Eq. (5) and assuming complete saturation for the neutrons, (v) varying γ by $\pm 10\%$, and (vi) assuming different parametrization for the fluctuations in the number of slow nucleons for a fixed N_{coll} value. We note that this uncertainty corresponds to the variation of the SNM parameters; therefore, it is meant as the uncertainty *within* our SNM and does not reflect any possible other model that could describe nucleus fragmentation. When using the N_{coll} values for the ZNA centrality estimator, the total systematic uncertainty on N_{coll} is obtained by adding the uncertainties from the Glauber and SNM parameters in quadrature.

Within the Glauber-model, the consistency between measurements of N_{coll} in largely separated rapidity regions establishes their relation to centrality. To this end, we correlate the ZNA measurements to the amplitudes measured in the innermost ring of the VZERO-A detector (VOA ring 1), since this ring covers the most-forward rapidity in the Pb-going direction. The N_{coll} distributions [$\mathcal{P}(N_{\text{coll}}|\text{cent}_{\text{ZNA}})$] for centrality classes selected with ZNA (cent_{ZNA}) are obtained from the SNM-Glauber fit. These are convolved with the NBD obtained from the NBD-Glauber fit to the MB VOA ring 1

distribution. Figure 6 compares the distributions of VOA ring 1 obtained from these convolutions to those measured in the same ZNA centrality classes. As expected, the distributions in the most-peripheral events, where the SNM does not provide a reliable description of the data, are not well reproduced by the Glauber-MC convolution. In all other classes, the experimental distributions are well reproduced. The deviations are consistent with those between $N_{\text{coll}}^{\text{ZNA}}$ (see Table III) and $N_{\text{coll}}^{\text{Pb-side}}$ (see Table VII) assuming that the target-going charged-particle multiplicity measured in VOA ring 1 is proportional to the number of wounded target nucleons.

In addition, Fig. 6 shows the results of an unfolding procedure. For each VOA ring 1 distribution selected by a ZNA centrality class, we find the N_{coll} distribution that, convolved with the NBD_{MB}, fits the data, i.e., the parameters of the fit are the relative contributions of each N_{coll} bin. The unfolded distributions (shown in blue) agree well with the data for all centrality bins, apart from a small discrepancy in the 80%-100% distribution at low amplitude, which is affected by trigger and event-selection efficiency. The $N_{\text{coll}}^{\text{MB}}$ distribution which results from the sum of the unfolded distributions of all centrality bins agree well with that from Glauber MC. The existence of N_{coll} distributions that, folded with NBD, agree with measured signal distributions is a necessary condition for ZNA to behave as an unbiased centrality selection. In contrast, it is worth noting that a centrality selection based on central multiplicity, as CL1, has no such solution; i.e., no such good agreement can be found when the VOA ring 1 distributions are selected by ordering the events according to CL1. The biases related to centrality selection will be discussed in the next

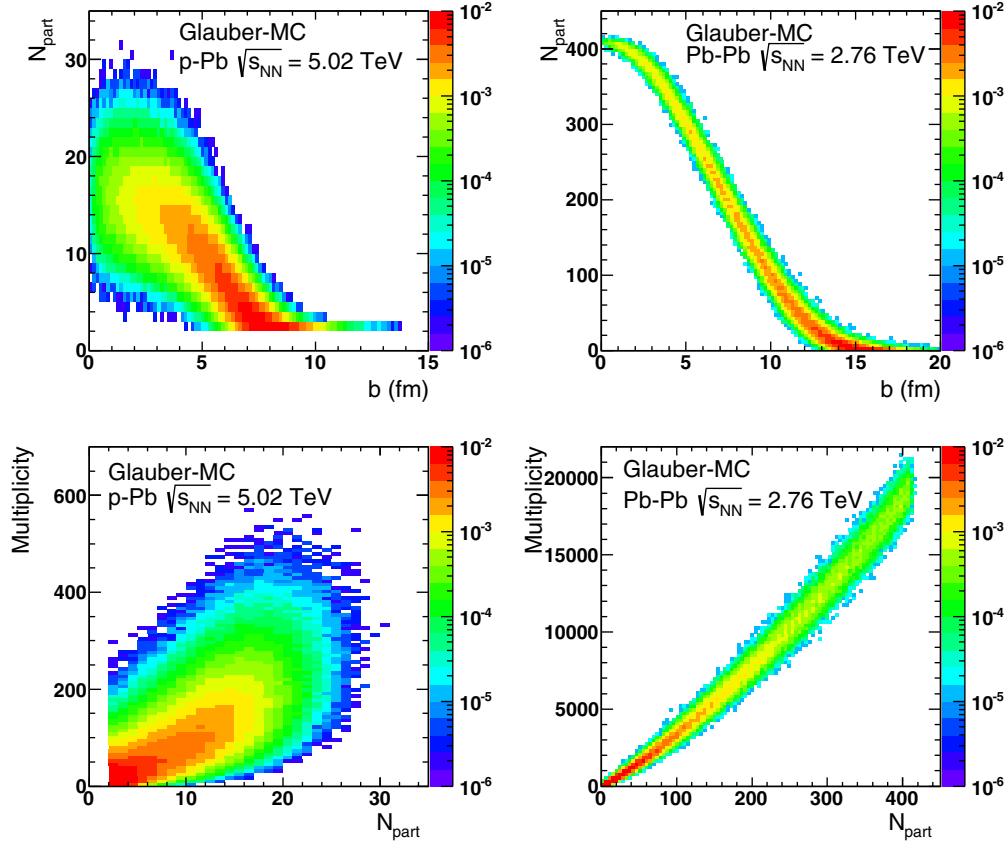


FIG. 7. (Color online) (top) Scatter plot of number of participating nucleons versus impact parameter. (bottom) Scatter plot of multiplicity versus the number of participating nucleons from the Glauber fit for V0A. The quantities are calculated with a Glauber Monte Carlo of p -Pb (left) and Pb-Pb (right) collisions.

section. The assumption that the ZNA selection is bias free will be used in Sec. VI as an ansatz for the hybrid method.

V. DISCUSSION OF POTENTIAL BIASES ON CENTRALITY

A. Multiplicity bias

Section III A describes the NBD-Glauber fitting procedure used to determine the collision geometry in terms of N_{coll} and N_{part} for each centrality class. The NBD is used to account for multiplicity fluctuations at fixed N_{part} . In contrast to Pb-Pb collisions, for p -Pb collisions these multiplicity fluctuations are sizable compared to the width of the N_{part} distribution, as illustrated in Fig. 7. For large fluctuations, a centrality classification of the events based on multiplicity may select a sample of nucleon-nucleon collisions which is biased compared to a sample defined by cuts on the impact parameter b .

This selection bias, which occurs for any system with large relative statistical fluctuations in particle multiplicity per nucleon-nucleon collision can be quantified by using the Glauber fit itself. The left panel of Fig. 8 shows the ratio between the average multiplicity per average participant and the average multiplicity of the NBD as a function of centrality. In Pb-Pb collisions, where the width of the plateau of the N_{part} distribution is large with respect to multiplicity fluctuations, the ratio deviates from unity only for the most peripheral

collisions. As expected, in p -Pb collisions the ratio differs from unity for all centralities with large deviations for the most central and most peripheral collisions; the most central (peripheral) collisions have on average much higher (lower) multiplicity per participant. When selecting event classes using impact parameter b intervals, there is no deviation from unity, as expected. The right panel of Fig. 8 shows, for each centrality estimator, the relative width of the NBD distribution (σ/μ). As expected, the estimators with the largest bias on the multiplicity per participant correspond to those with the largest relative width.

It is instructive for the further discussion to consider the clan model [53], which is the standard physical explanation of the NBD distribution in the context of particle production in pp collisions. In this model particle sources, called ancestors, are produced independently according to a Poisson distribution with mean value, $\langle N \rangle = k \ln(1 + \mu/k)$. Each ancestor can produce on average $\mu/\langle N \rangle$ particles, e.g., by decay and fragmentation, and a clan contains all particles that stem from the same ancestor. Hence, the bias observed above also corresponds to a biased number of clans, which are sources of particle production. Analogously, in all recent Monte Carlo generators a large part of the multiplicity fluctuations is indeed due to the fluctuations of the number of particle sources, i.e., multiple semihard ($Q^2 \gg \Lambda_{\text{QCD}}^2$) parton-parton scatterings (MPI).

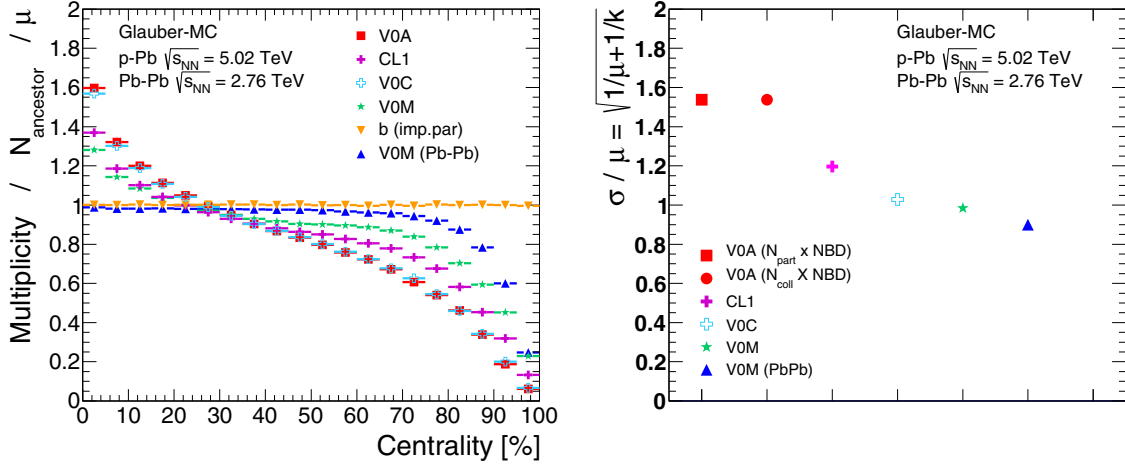


FIG. 8. (Color online) (left) Multiplicity fluctuation bias quantified as the mean multiplicity per $\langle N_{\text{par}} \rangle / \mu$ from the NBD-Glauber MC in $p\text{-Pb}$ and Pb-Pb calculations. (right) Relative width of the NBD obtained from the NBD-Glauber fit of various multiplicity distributions in $p\text{-Pb}$ and Pb-Pb calculations.

As an example, the HIJING generator accounts for fluctuations of the number of MPI per NN interaction via a NN overlap function $T_{NN}(b_{NN})$, where b_{NN} is the NN impact parameter, i.e., the impact parameter between the proton and each wounded nucleon of the Pb nucleus. The probability for inelastic NN collisions is given as one minus the probability to have no interaction:

$$d\sigma_{\text{inel}} = \pi d b_{NN}^2 [1 - e^{-(\sigma_{\text{soft}} + \sigma_{\text{hard}}) T_{NN}(b_{NN})}], \quad (6)$$

where σ_{soft} is the geometrical soft cross section of 57 mb [29] related to the proton size and σ_{hard} is the energy-dependent pQCD cross section for $2 \rightarrow 2$ parton scatterings. Furthermore, as in the clan model, there is a Poissonian probability

$$P(n_{\text{hard}}) = \frac{\langle n_{\text{hard}} \rangle^{n_{\text{hard}}}}{n_{\text{hard}}!} e^{-\langle n_{\text{hard}} \rangle} \quad (7)$$

for multiple hard collisions with an average number determined by b_{NN} :

$$\langle n_{\text{hard}} \rangle = \sigma_{\text{hard}} T_{NN}(b_{NN}). \quad (8)$$

Hence, the biases on the multiplicity discussed above correspond to a bias on the number of hard scatterings (n_{hard}) and $\langle b_{NN} \rangle$ in the event. The latter correlates fluctuations over large rapidity ranges (long-range correlations). As a consequence, for peripheral (central) collisions we expect a lower (higher) than average number of hard scatterings per binary collision, corresponding to a nuclear modification factor less than one (greater than one).

In general, the number of binary pN collisions, $\langle N_{\text{coll}} \rangle$, is used to scale the reference pp yields and obtain the nuclear modification factor, which is used to quantify nuclear matter effects. However, for centrality classes based on multiplicity, owing to the bias induced by such selection, hard processes do not simply scale with N_{coll} but rather with an effective number of collisions, obtained by scaling the $\langle N_{\text{coll}}^{\text{Glauber}} \rangle$ by the number of hard scatterings per pN collision: $\langle N_{\text{coll}}^{\text{Glauber}} \rangle \langle n_{\text{hard}} \rangle_{pN} / \langle n_{\text{hard}} \rangle_{pp}$. As discussed in the HIJING example above, the number of hard scatterings per

pN collision is simulated in Monte Carlo models. In this specific MC, even without bias, the total number of hard scatterings deviates from simple N_{coll} scaling due to energy conservation at high N_{coll} . Instead, with the objective to study a baseline corresponding to an incoherent and unconstrained superposition of nucleon-nucleon collisions, the PYTHIA [54] event generator has been coupled to the $p\text{-Pb}$ MC Glauber calculation. For each MC Glauber event PYTHIA is used to generate N_{coll} independent pp collisions. In the following we refer to this model as G-PYTHIA. In this model, the number of hard scatterings per pN collision shows a strong deviation from N_{coll} scaling which is illustrated in Fig. 9 and resembles the bias observed in Fig. 8.

B. Jet-veto bias

Additional kinematic biases exist for events containing high- p_T particles. These particles arise from the fragmentation

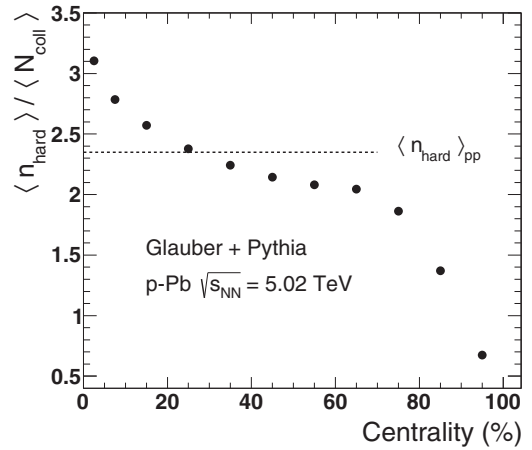


FIG. 9. Number of hard scatterings [MSTI(31) in PYTHIA6] per N_{coll} as a function of the centrality calculated with a toy MC that couples a pp PYTHIA6 calculation to a $p\text{-Pb}$ Glauber MC (described in the text).

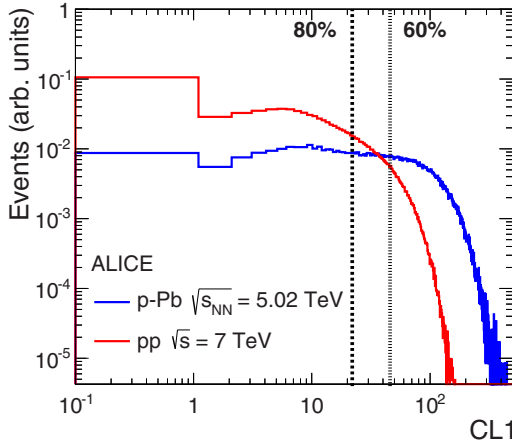


FIG. 10. (Color online) Multiplicity distribution used as centrality estimators in p -Pb collisions, compared to the distribution in pp collisions at $\sqrt{s} = 7$ TeV. The dashed lines mark the 80% and the 60% percentile of the p -Pb cross section, respectively.

of partons produced in parton-parton scattering with large momentum transfer. Their contribution to the overall multiplicity rises with parton energy and, thus, can introduce a trivial correlation between the centrality estimator and the presence of a high- p_T particle in the event. In particular, for very peripheral collisions, the multiplicity range that governs the centrality for the bulk of soft collisions can represent an effective veto on hard processes, leading to a $R_{p\text{Pb}} < 1$. This bias is illustrated in Fig. 10. It shows a multiplicity distribution which is used as centrality estimators in p -Pb collisions, compared to the same distribution in pp collisions at $\sqrt{s} = 7$ TeV. The dashed lines mark the 80%–100% (60%–100%) p -Pb multiplicity cut is 0.8 (0.97). The 80% cut in p -Pb is smaller than the multiplicity range covered in pp , therefore resulting in an effective veto on the large multiplicity events produced by hard processes.

C. Geometric bias

The b_{NN} dependence of particle production postulated in Sec. V A leads to a purely geometrical centrality estimator independent bias for peripheral p -Pb collisions [55]. As illustrated in Fig. 11, the mean impact parameter between two nucleons (b_{NN}), calculated from a Monte Carlo Glauber simulation, is almost constant for central collisions, but rises significantly for $N_{\text{part}} < 6$. This reduces the average number of MPIs for most peripheral events, enhancing the effect of the bias leading to a nuclear modification factor less than (greater than) one for peripheral (central) collisions.

In summary, based on simplified models we have identified three different possible biases that are expected to lead to deviations from unity at high p_T of the nuclear modification factors in peripheral and central collisions. As will be discussed and studied in the following sections, the effect decreases with increasing rapidity separation between the $R_{p\text{Pb}}$ measurement and the centrality estimator.

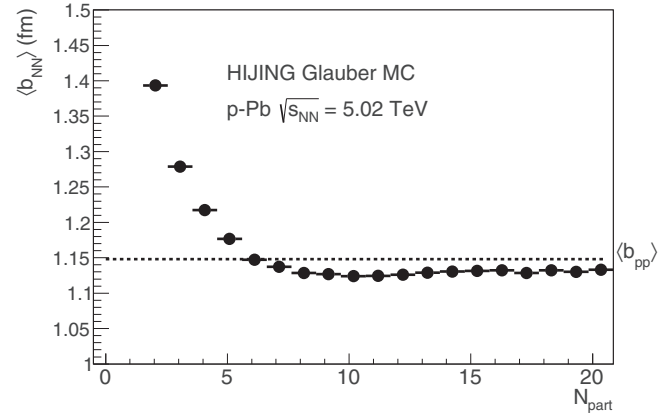


FIG. 11. Average nucleon-nucleon impact parameter as a function of the number of participants for p -Pb at $\sqrt{s_{NN}} = 5.02$ TeV from a Glauber MC calculation as implemented in HIJING (no shadowing, no elastic scattering). The result depends on the modeling of the spatial parton density in the nucleon. In HIJING it is approximated by the Fourier transform of a dipole form factor.

For the estimators we used, the main biases are

- (i) CL1: strong bias due to the full overlap with tracking region. Additional bias from the “jet veto effect,” as jets contribute to the multiplicity and shift events to higher centralities (p_T dependent);
- (ii) V0M: reduced bias since the VZERO hodoscopes are outside the tracking region;
- (iii) V0A: reduced bias because of the enhanced contribution from the Pb fragmentation region;
- (iv) ZNA: no bias expected.

In addition, independent of the centrality estimator, there is a geometrical bias for peripheral collisions (see Sec. V C).

VI. THE HYBRID METHOD

A. Basis and assumptions of the method

The hybrid method presented in the following section aims to provide an unbiased centrality estimator and relies on two main assumptions. The first is to assume that an event selection based on ZN does not introduce any bias on the bulk at midrapidity and on high- p_T particle production. This assumption is based on the results from the unfolding procedure presented in Sec. IV and the full acceptance of ZN for neutrons emitted from the Pb nucleus, also discussed in Sec. IV. In addition consistent results were obtained with proton calorimeter ZP, in the region of its full acceptance. Therefore, we do not expect a significant bias from the ZN selection and herein this is taken as ansatz. This selection was also used in the method proposed in Sec. IV; however, the N_{coll} determination provided by the SNM-Glauber model is model dependent. In contrast, in the hybrid method, the N_{coll} determination is based—as an ansatz—on a particular scaling for particle multiplicity (the second assumption), e.g., we assume that the charged-particle multiplicity measured at midrapidity scales with the number of participants.

TABLE VI. Average pseudorapidity covered by VZERO detector rings in p -Pb and Pb- p collisions.

Ring	$\langle \eta_{\text{cms}} \rangle (p\text{-Pb})$	$\langle \eta_{\text{cms}} \rangle (\text{Pb-}p)$
VZERO-A ring 1	-5.39	4.45
VZERO-A ring 2	-4.80	3.87
VZERO-A ring 3	-4.28	3.35
VZERO-A ring 4	-3.82	2.89
VZERO-C ring 1	3.34	-4.26
VZERO-C ring 2	2.82	-3.74
VZERO-C ring 3	2.33	-3.25
VZERO-C ring 4	1.86	-2.78

To obtain more insight into the particle-production mechanisms, we study the correlation of various pairs of observables that, in ZN-centrality classes, are expected to scale linearly with N_{part} or N_{coll} . One of these observables is the charged-particle density $dN_{\text{ch}}/d\eta$ in $|\eta| < 2.0$, measured with the SPD. The charged-particle pseudorapidity density is obtained from the measured distribution of tracklets, formed by using the position of the primary vertex and two hits, one on each SPD layer [24]. At larger pseudorapidities, where a direct multiplicity measurement is not available, we study the raw signals of the four rings of the VZERO-A and VZERO-C detectors separately. We exploit both beam configurations, p -Pb and Pb- p , in order to cover the widest possible rapidity range. To take into account the impact of secondary particles, the pseudorapidity coverage of the VZERO detector rings with respect to the primary charged particles was calculated with a full detector simulation based on DPMJET [51,52] and it is given in Table VI in the center-of-mass system (cms), which moves with a rapidity of $\Delta y_{NN} = 0.465$ in the direction of the proton beam (see Sec. II).

The information about charged-particle multiplicity, dominated by soft particles, is complemented with observables from hard processes which are expected to scale with the number of binary collisions, such as the yield of high- p_T

($10 < p_T < 20$ GeV/ c) particles measured at midrapidity ($|\eta| < 0.3$).

In order to compare these observables on the same scale and also, at first order, to neglect detector efficiency and acceptance effects, we use so-called normalized signals $\langle S \rangle_i / \langle S \rangle_{\text{MB}}$. These are obtained dividing $\langle S \rangle_i$, i.e., the mean value of $dN_{\text{ch}}/d\eta$, number of raw SPD tracklets or raw VZERO signal in a given ZN-centrality class i , by the corresponding mean values in minimum-bias collisions.

Figure 12 shows, for bins in ZN centrality, the correlation between a few selected normalized signals and the normalized charged-particle density averaged over $-1 < \eta < 0$. The statistical uncertainty is negligible, while the systematic uncertainties largely cancel in the ratio to the MB signals. One can note that the correlation exhibits a clear dependence on the pseudorapidity of the normalized signal. The slope of the normalized signals with $dN_{\text{ch}}/d\eta$ diminishes towards the proton direction (C side in p -Pb collisions). For example, in the innermost ring of the VZERO-C detector the signal amplitude range is about a factor three, while for the innermost ring of the VZERO-A detectors it is about twice as large.

In the wounded nucleon model [18], the total number of participants N_{part} is expressed in terms of target and projectile participants. The charged-particle density at midrapidity is thus proportional to N_{part} , whereas at higher rapidities the model predicts a dependence on a linear combination of the number of target and projectile participants with coefficients which depend on the rapidity. Close to Pb-rapidity a linear wounded target nucleon scaling ($N_{\text{part}}^{\text{target}} = N_{\text{part}} - 1$) is expected.

In order to further understand the relative trends of the observables in Fig. 12 and to relate them with geometrical quantities, such as N_{part} , one can adopt the wounded nucleon model and make the assumption that $dN_{\text{ch}}/d\eta$ in $-1 < \eta < 0$ is proportional to N_{part} . In this case, the other observables can be related to N_{part} , assuming linear or power-law dependence. The linear dependence can be parametrized with $N_{\text{part}} - \alpha$, where α is a free parameter. Then the normalized signals can

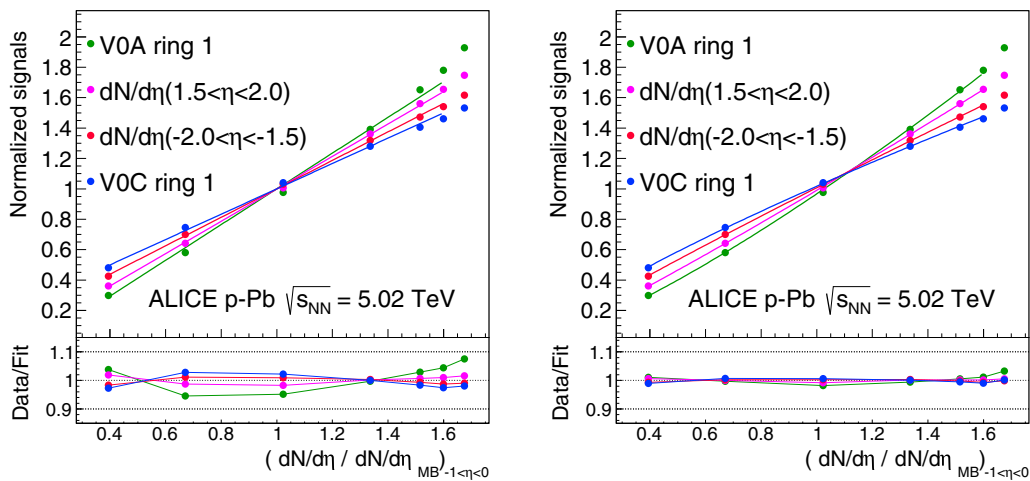


FIG. 12. (Color online) (left) Normalized signal from various observables (the innermost ring of VZERO-A and VZERO-C and two rapidity intervals of $dN_{\text{ch}}/d\eta$) versus the normalized charged-particle density averaged over $-1 < \eta < 0$. (left) Fit with the linear function from Eq. (9). (right) Fit with the power-law function from Eq. (10). Only data from p -Pb collisions are shown.

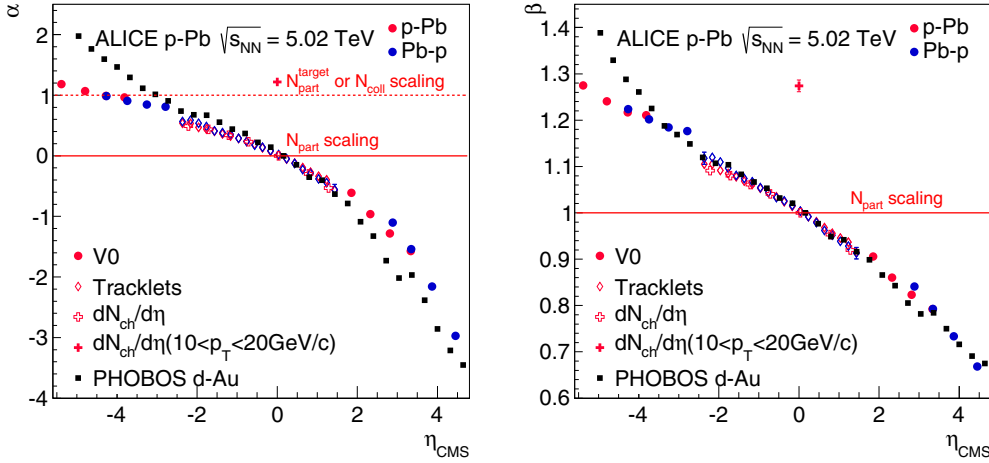


FIG. 13. (Color online) Results from the fits of Eqs. (9) (left) and (10) (right) of the normalized signals as a function of the pseudorapidity covered by the various observables. The red horizontal lines (left) indicate the ideal N_{part} and N_{coll} geometrical scalings. For the PHOBOS data, η_{cms} has been scaled by the ratio of the beam rapidities in $p\text{-Pb}$ at $\sqrt{s_{\text{NN}}} = 5.02 \text{ TeV}$ and $d\text{-Au}$ collisions at $\sqrt{s_{\text{NN}}} = 200 \text{ GeV}$.

be expressed with $(N_{\text{part}} - \alpha)/(N_{\text{part}} - \alpha)$ and one obtains the following linear relation:

$$\frac{\langle S \rangle_i}{\langle S \rangle_{\text{MB}}} = \frac{\langle N_{\text{part}} \rangle_{\text{MB}}}{(\langle N_{\text{part}} \rangle_{\text{MB}} - \alpha)} \left(\frac{\langle dN/d\eta \rangle_i}{\langle dN/d\eta \rangle_{\text{MB}}} \right)_{-1 < \eta < 0} - \frac{\alpha}{(\langle N_{\text{part}} \rangle_{\text{MB}} - \alpha)}, \quad (9)$$

where $\langle N_{\text{part}} \rangle_{\text{MB}} = 7.9$ is the average number of participating nucleons in minimum-bias collisions. The relation is used to find α for each observable by a fit to the data. Analogously, we can also fit a power-law function as

$$\begin{aligned} \frac{\langle S \rangle_i}{\langle S \rangle_{\text{MB}}} &= \left(\frac{\langle dN/d\eta \rangle_i^\beta}{\sum_i w_i \langle dN/d\eta \rangle_i^\beta} \right)_{-1 < \eta < 0} \\ &= \left(\frac{\langle dN/d\eta \rangle_i^\beta}{\langle \langle dN/d\eta \rangle^\beta \rangle_{\text{MB}}} \right)_{-1 < \eta < 0}, \end{aligned} \quad (10)$$

where the w_i are the width of the centrality classes and β is a fit parameter. Since we made the assumption that $dN_{\text{ch}}/d\eta$ in $-1 < \eta < 0$ is proportional to N_{part} , β obtained from Eq. (10) equivalently quantifies the deviations from a perfect N_{part} ($\beta = 1$) scaling. As can be seen from the lower panels of Fig. 12, the power-law fit describes the data better, especially for the observables located further away from midrapidity. This also means that the linear dependence assumed in Eq. (9) can only be valid approximately.

Figure 13 shows the results of the fits in Eqs. (9) and (10) as a function of η_{cms} of the measured observables. The figure displays data collected in both $p\text{-Pb}$ and $\text{Pb-}p$ beam configurations. Since the $\text{Pb-}p$ data were taken at high-luminosity (reaching 200 kHz, roughly corresponding to a luminosity of $10^{29} \text{ s}^{-1} \text{ cm}^{-2}$), the results are affected by interaction pileup (probability per bunch crossing between 3.8%–4.3%). In order to reduce the effect of the pileup and to treat $p\text{-Pb}$ and $\text{Pb-}p$ data consistently, we excluded the 0%–5% centrality class from the fits. Furthermore, in order to take into account the remaining distortions in the 5%–100% classes, the $\text{Pb-}p$ data

were corrected by using the results for the tracklets (also shown in Fig. 13) in a small η region, ($|\eta_{\text{lab}}| < 0.2$), where $|\eta_{\text{cms}}|$ is nearly identical for $p\text{-Pb}$ and $\text{Pb-}p$ configurations. Typically, the absolute correction is 0.05 and 0.01 for the α and β parameters, respectively.

The results presented in Fig. 13 indicate a smooth and continuous change of the scaling behavior for charged-particle production with pseudorapidity. It is worth noting that, at large negative pseudorapidity (Pb-going direction), the values of the parameters α and β reach those obtained for charged-particle production at high p_{T} . In contrast, the parameter values are much lower in the proton-going direction. Our data are overlaid with the corresponding fit parameters derived from PHOBOS charged-particle multiplicity measurements in $d\text{-Au}$ collisions at $\sqrt{s_{\text{NN}}} = 200 \text{ GeV}$ [21]. The normalized charged-particle multiplicity in each pseudorapidity bin is fit against $(\frac{\langle dN/d\eta \rangle_i}{\langle dN/d\eta \rangle_{\text{MB}}})_{|\eta| < 0.1}$ using Eqs. (9) and (10). The results obtained in this way are then adjusted by scaling the x axis (η_{cms}) by the ratio of the beam rapidities in $p\text{-Pb}$ at $\sqrt{s_{\text{NN}}} = 5.02 \text{ TeV}$ and $d\text{-Au}$ collisions at $\sqrt{s_{\text{NN}}} = 200 \text{ GeV}$. The comparison between PHOBOS and our data shows a good agreement over a wide η range, with some deviations at large negative pseudorapidity. In particular, the η region covered by the innermost ring of the VZERO-A detector corresponds to the target fragmentation region where extended longitudinal scaling was observed at RHIC [21]. The minimum bias N_{part} and N_{coll} are obtained by PHOBOS relying on a tuned HIJING-based Monte Carlo simulation [21].

B. Calculation of $\langle N_{\text{coll}} \rangle$

As discussed in the previous section, selecting the events using the ZN signal is expected to be free from bias on the bulk multiplicity or high- p_{T} particle yields. In order to establish a relationship to the collision geometry, we exploit the findings from the correlation analysis described above and make use of observables that are expected to scale as a linear function of N_{coll} or N_{part} .

Three sets of $\langle N_{\text{coll}} \rangle$ values are calculated, based on the following assumptions:

- (i) $N_{\text{coll}}^{\text{mult}}$: the charged-particle multiplicity at midrapidity is proportional to the number of participants (N_{part});
- (ii) $N_{\text{coll}}^{\text{high-}p_{\text{T}}}$: the yield of charged high- p_{T} particles at midrapidity is proportional to the number of binary NN collisions (N_{coll});
- (iii) $N_{\text{coll}}^{\text{Pb-side}}$: the target-going charged-particle multiplicity is proportional to the number of wounded target nucleons ($N_{\text{part}}^{\text{target}} = N_{\text{part}} - 1 = N_{\text{coll}}$).

For the charged-particle multiplicity in the Pb-going side we use the signal from the innermost ring of the VZERO-A detector. We note that assumptions (1) and (2) are satisfied for minimum-bias collisions, where we measured a value of $(dN_{\text{ch}}/d\eta_{\text{cms}})/\langle N_{\text{part}} \rangle$ consistent with that in inelastic pp collisions (0.97 ± 0.08) [24] and an integrated $R_{pA}(10 < p_{\text{T}} < 20 \text{ GeV}/c) = 0.995 \pm 0.010 \text{ (stat.)} \pm 0.090 \text{ (syst.)}$ (see Sec. VII).

Therefore, in order to obtain the average number of binary NN collisions in each centrality interval, the minimum-bias value of $\langle N_{\text{part}} \rangle_{\text{MB}} = 7.9$ is scaled by using the ratio of the multiplicity at midrapidity:

$$\langle N_{\text{part}} \rangle_i^{\text{mult}} = \langle N_{\text{part}} \rangle_{\text{MB}} \left(\frac{\langle dN/d\eta \rangle_i}{\langle dN/d\eta \rangle_{\text{MB}}} \right)_{-1 < \eta < 0}, \quad (11)$$

$$\langle N_{\text{coll}} \rangle_i^{\text{mult}} = \langle N_{\text{part}} \rangle_i^{\text{mult}} - 1. \quad (12)$$

In a similar way the minimum-bias value of $\langle N_{\text{coll}} \rangle_{\text{MB}} = 6.9$ is scaled by using the ratio of the yield of high- p_{T} particles at midrapidity to obtain $N_{\text{coll}}^{\text{high-}p_{\text{T}}}$:

$$\langle N_{\text{coll}} \rangle_i^{\text{high-}p_{\text{T}}} = \langle N_{\text{coll}} \rangle_{\text{MB}} \frac{\langle S \rangle_i}{\langle S \rangle_{\text{MB}}}, \quad (13)$$

where S stands for the charged-particle yields with $10 < p_{\text{T}} < 20 \text{ GeV}/c$. Alternatively, one can use the Pb-side multiplicity to obtain $N_{\text{coll}}^{\text{Pb-side}}$:

$$\langle N_{\text{coll}} \rangle_i^{\text{Pb-side}} = \langle N_{\text{coll}} \rangle_{\text{MB}} \frac{\langle S \rangle_i}{\langle S \rangle_{\text{MB}}} \quad (14)$$

where S stands for the raw signal of the innermost ring of VZERO-A. The obtained values of $\langle N_{\text{coll}} \rangle$ in ZNC-centrality classes are listed in Table VII and shown in Fig. 14.

The systematic uncertainty is given by the 8% uncertainty on the $\langle N_{\text{coll}} \rangle_{\text{MB}}$ (or the 3.4% uncertainty on the $\langle T_{p\text{Pb}} \rangle_{\text{MB}}$)

TABLE VII. $\langle N_{\text{coll}} \rangle$ values obtained under the three assumptions discussed in the text.

Centrality (%)	$N_{\text{coll}}^{\text{mult}}$	$N_{\text{coll}}^{\text{high-}p_{\text{T}}}$	$N_{\text{coll}}^{\text{Pb-side}}$
0–5	12.2	12.5	13.3
5–10	11.6	12.1	12.3
10–20	11.0	11.3	11.4
20–40	9.56	9.73	9.60
40–60	7.08	6.81	6.74
60–80	4.30	4.05	4.00
80–100	2.11	2.03	2.06

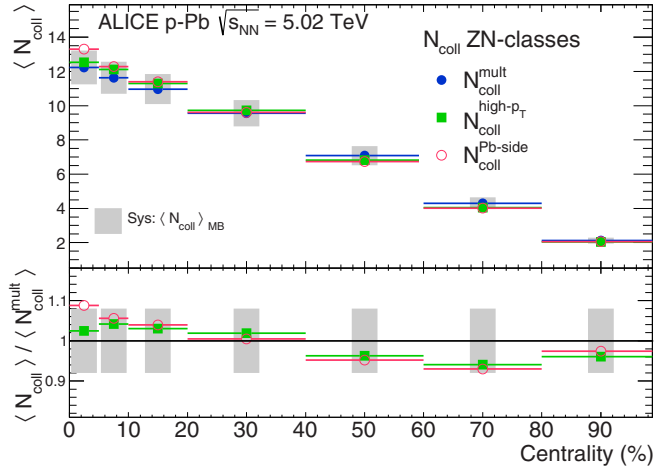


FIG. 14. (Color online) $\langle N_{\text{coll}} \rangle$ values obtained with the hybrid method under the three assumptions discussed in the text. The systematic uncertainty, shown as a gray band around the $N_{\text{coll}}^{\text{mult}}$ points, represents the 8% uncertainty on the $\langle N_{\text{coll}} \rangle_{\text{MB}}$.

listed in Table III. We assign no uncertainty to the assumptions made for particle scaling. The differences between the three sets of values do not exceed 9% in all centrality classes. This confirms the consistency of the assumptions used, but it does not prove that any (or all) of the assumptions are valid. We note that these values, in particular $N_{\text{coll}}^{\text{Pb-side}}$, agree within 18% with those calculated with the SNM (see Fig. 2 and Table III), except for the most peripheral reactions, where the SNM is inaccurate.

In addition, we plot in Fig. 15 the zero-degree signal from neutral particles in the proton-going direction ZNC vs $N_{\text{coll}}^{\text{mult}}$. We have excluded events without a signal in the ZNC; however, the qualitative trend does not change when including those events. Over a wide range of centralities (10%–100%) a linear anticorrelation is observed. This is consistent with a

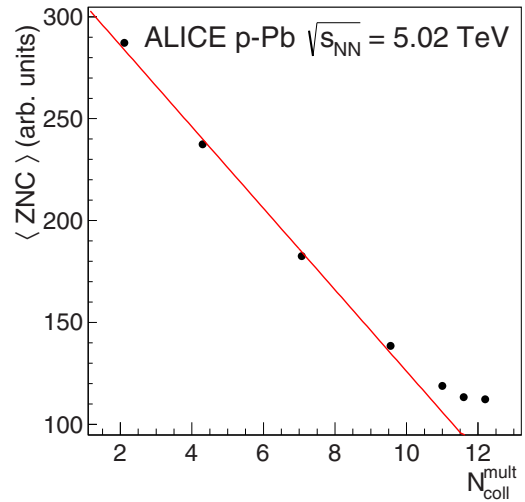


FIG. 15. (Color online) Signal in the proton-going direction ZNC as a function of $N_{\text{coll}}^{\text{mult}}$. The red line shows a linear fit to the first four data points.

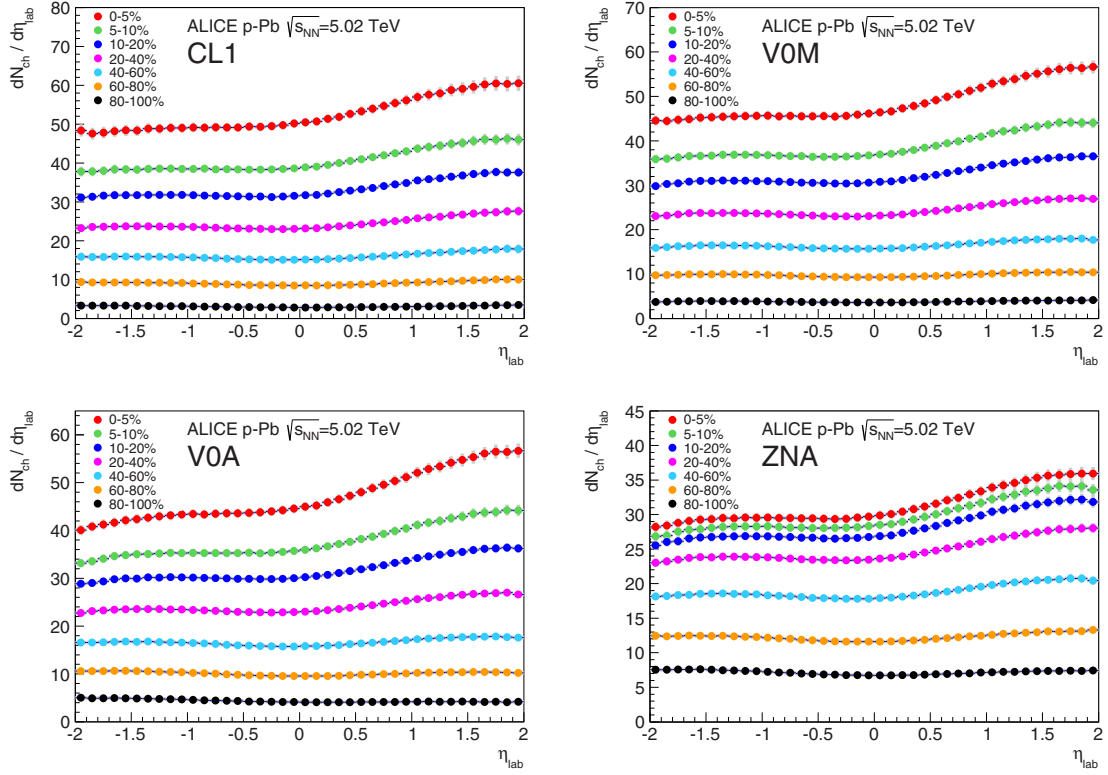


FIG. 16. (Color online) Pseudorapidity density of charged particles measured in p -Pb collisions at $\sqrt{s_{NN}} = 5.02$ TeV for various centrality classes and estimators. The different panels correspond to different centrality estimators: CL1 (top left), VOM (top right), VOA (bottom left), ZNA (bottom right).

longitudinal energy transfer of the proton proportional to the number of binary collisions.

VII. RESULTS AND IMPLICATIONS FOR PARTICLE PRODUCTION

A. Charged-particle density

The measurement of the centrality dependence of the particle multiplicity density allows a discrimination between models that describe the initial state of heavy-ion collisions. In Ref. [24] we described the charged-particle pseudorapidity density in minimum-bias collisions. The same analysis was repeated, dividing the visible cross section (see Sec. II) into event classes defined by the centrality estimators described above, and the $\langle N_{\text{part}} \rangle$ values associated with each centrality interval were calculated by using the methods discussed in Secs. III A, IV, and VI.

The results of the charged-particle multiplicity density as a function of the pseudorapidity are presented in Fig. 16 for different centrality intervals and different centrality estimators. The fully correlated systematic uncertainty, is given by the quadrature sum of the 2.2% minimum bias error detailed in Ref. [24], and an η -dependent uncertainty from the vertex efficiency and the centrality selection.

In peripheral collisions (60%–80% and 80%–100%) the shape of the distribution is almost fully symmetric and resembles what is seen in proton-proton collisions. In more central collisions, the shape of $dN_{\text{ch}}/d\eta$ becomes progressively more asymmetric, with an increasing excess of particles produced

in the direction of the Pb beam compared to the proton-going direction. The shape of the pseudorapidity density function is sensitive to details of particle production models. For example, it was found in Ref. [24] that in minimum-bias reactions the η_{lab} dependence is described relatively well by HIJING [56] or DPMJET [52], with a gluon shadowing parameter tuned to describe experimental data at lower energy, whereas the saturation models [57–59] exhibit a steeper η_{lab} dependence than the data. We have quantified the centrality evolution of the pseudorapidity shape for the different centrality estimators by analyzing the density at midrapidity, and the asymmetry of particle yield between the proton and the Pb peak regions, as the ratio of $dN_{\text{ch}}/d\eta$ at $0 < \eta < 0.5$ and $-1.5 < \eta < -1.0$, symmetrically around the center of mass. This is shown in Fig. 17.

Figure 18 shows the $dN_{\text{ch}}/d\eta$ integrated at midrapidity divided by the number of participants as a function of $\langle N_{\text{part}} \rangle$ (left) or as a function of $dN_{\text{ch}}/d\eta$ (right) for various centrality estimators. The systematic uncertainty is smaller than the marker size. For the VOA centrality estimator, in addition to the $\langle N_{\text{part}} \rangle$ from the standard Glauber calculation, the results obtained with the implementation of Glauber–Gribov model (with $\Omega = 0.55$) are also shown. For CL1, VOM, and VOA, the charged-particle density at midrapidity has a steeper-than-linear increase, as a consequence of the strong multiplicity bias discussed in Sec. V, which is strongest in CL1, where the overlap with the tracking region is maximum. This trend is not seen in the case of the Glauber–Gribov model, which shows a relatively constant behavior for the integrated

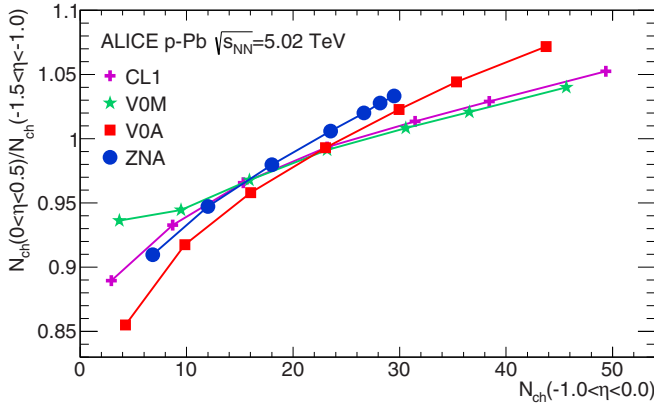


FIG. 17. (Color online) Asymmetry of particle yield, calculated as the ratio of the pseudorapidity density integrated in $0 < \eta < 0.5$ to that in $-1.5 < \eta < -1$ as a function of the pseudorapidity density integrated at midrapidity for various centrality classes and estimators.

yield divided by the number of participant pairs, with the exception of the most peripheral point.

For ZNA, there is a clear sign of saturation above $N_{\text{part}} \sim 10$, as the $\langle N_{\text{part}} \rangle$ values are closer to each other. Most probably, this is due to the saturation of forward neutron emission. We note that none of these curves point towards the pp data point. This suggests that the geometry bias, present in peripheral collisions, together with the multiplicity bias for CL1, VOM, and VOA, has a large effect on this centrality class.

In contrast, the results obtained with the hybrid method, where the $N_{\text{part}}^{\text{Pb-side}}$ and the $N_{\text{part}}^{\text{high-}p_T}$ give very similar trends, show, within $\pm 10\%$, scaling with N_{part} , which naturally reaches the pp point, well within the quoted uncertainty of 8% on the N_{part} values. In addition, they show that the range in N_{part} covered with an unbiased centrality selection is more limited than what is obtained by using estimators based on particle multiplicity. The latter do not select on the collision geometry but rather on the final products of the collision. This effect is emphasized in the right plot, which shows the same quantity N_{ch} divided by N_{part} as a function of N_{ch} . Here the limited

range in N_{ch} reached with the ZNA selection is clearly visible. This indicates the sensitivity of the N_{part} -scaling behavior to the Glauber modeling, as well as the importance of the multiplicity fluctuations.

B. Nuclear modification factors

As discussed in Sec. V, the various centrality estimators induce a bias on the nuclear modification factor depending on the rapidity range they cover. In contrast to minimum-bias collisions, where $\langle N_{\text{coll}} \rangle = 6.9$ is fixed by the ratio of the pN and $p\text{-Pb}$ cross sections, in general, N_{coll} for a given centrality class cannot be used to scale the pp cross section or to calculate centrality-dependent nuclear modification factors. For a centrality selected event sample, we therefore define $Q_{p\text{-Pb}}$ as

$$\begin{aligned} Q_{p\text{-Pb}}(p_T; \text{cent}) &= \frac{dN_{\text{cent}}^{p\text{-Pb}}/dp_T}{\langle N_{\text{coll}}^{\text{Glauber}} \rangle dN^{pp}/dp_T} \\ &= \frac{dN_{\text{cent}}^{p\text{-Pb}}/dp_T}{\langle T_{p\text{-Pb}}^{\text{Glauber}} \rangle d\sigma^{pp}/dp_T} \end{aligned} \quad (15)$$

for a given centrality percentile according to a particular centrality estimator. In our notation we distinguish $Q_{p\text{-Pb}}$ from $R_{p\text{-Pb}}$ because the former is influenced by potential biases from the centrality estimator which are not related to nuclear effects. Hence, $Q_{p\text{-Pb}}$ can be different from unity even in the absence of nuclear effects.

The p_T distribution of primary charged particles in minimum-bias collisions is given in Ref. [60]. The charged-particle spectra are reconstructed with the two main ALICE tracking detectors, the Inner Tracking System and the Time Projection Chamber, and are corrected for the detector and reconstruction efficiency using a Monte Carlo simulation based on the DPMJET event generator [52]. The systematic uncertainties on corrections are estimated via a comparison to a Monte Carlo simulation by using the HIJING event generator [29], while the p_T resolution is estimated from the space-point residuals to the track fit and verified with data. The total systematic uncertainty ranges between 3.4%

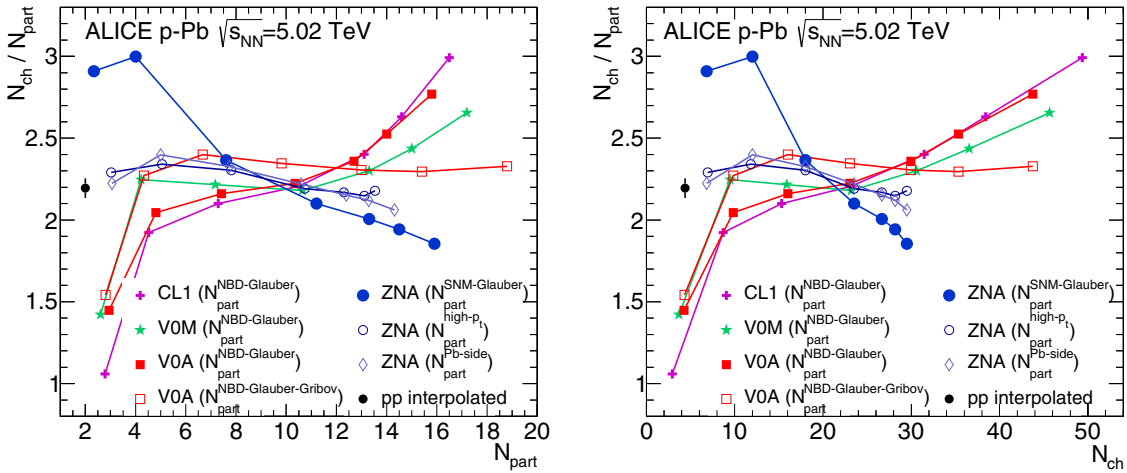


FIG. 18. (Color online) Pseudorapidity density of charged particles measured in $p\text{-Pb}$ collisions at midrapidity per participant as a function of N_{part} (left), or as a function of the midrapidity density (right), for various centrality estimators.

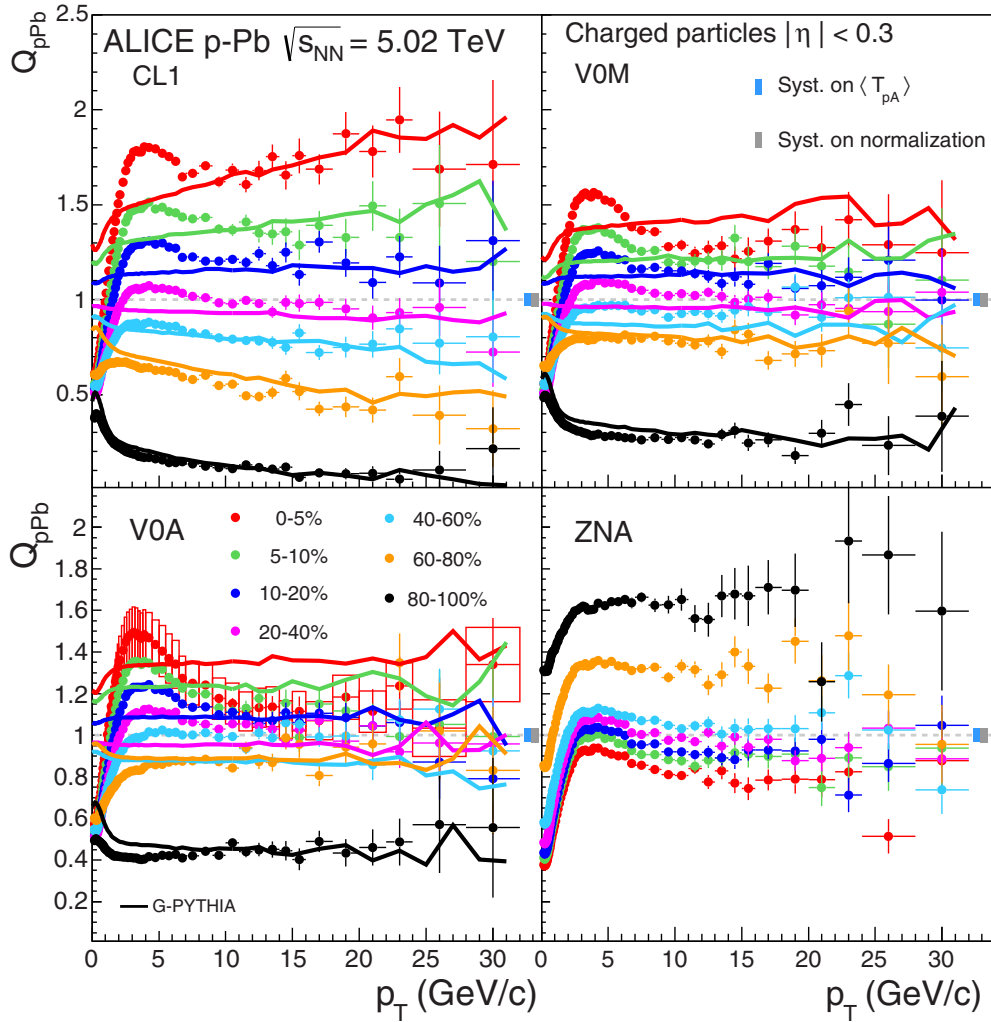


FIG. 19. (Color online) $Q_{p\text{Pb}}$ spectra (points) of all primary charged particles for various centrality classes obtained with the different centrality estimators explained in the text. The lines are from G-PYTHIA calculations. The systematic error on the spectra is only shown for the VOA 0%–5% centrality bin and is the same for all others. The systematic uncertainty on pp and $p\text{-Pb}$ normalization is shown as a gray box around unity at $p_T = 0$. The systematic uncertainty on $\langle T_{p\text{Pb}} \rangle_{\text{MB}}$ is shown as a light blue box around unity at high p_T .

and 6.7% in the measured p_T range, 0.15–50 GeV/c, with a negligible η_{cms} dependence. The nuclear modification factor is calculated by dividing the data by the reference pp spectrum scaled by $\langle N_{\text{coll}} \rangle_{\text{MB}}$. The reference pp spectrum is obtained at low p_T ($p_T < 5$ GeV/c) by interpolating the data measured at $\sqrt{s} = 2.76$ and 7 TeV, and at high p_T ($p_T > 5$ GeV/c) by scaling the measurements at $\sqrt{s} = 7$ TeV with the ratio of spectra calculated with NLO pQCD at $\sqrt{s} = 5.02$ and 7 TeV [61]. The systematic uncertainty, given by the largest of the relative systematic uncertainties of the spectrum at 2.76 or 7 TeV at low p_T and assigned from the relative difference between the NLO-scaled spectrum for different scales and the difference between the interpolated and the NLO-scaled data at high p_T , ranges from 6.8% to 8.2%. For MB collisions the nuclear modification factor $R_{p\text{Pb}}$ is consistent with unity for p_T above 6 GeV/c.

The same analysis was repeated by dividing the visible cross section (see Sec. II) in event classes defined by the centrality estimators described above, and the $Q_{p\text{Pb}}$ were calculated by

using the values of $\langle N_{\text{coll}} \rangle$ listed in Tables III and VII for each given estimator. Figure 19 shows $Q_{p\text{Pb}}$ for different centrality estimators and different centrality classes. The uncertainties of the $p\text{-Pb}$ and pp spectra are added in quadrature, separately, for the statistical and systematic uncertainties. The systematic uncertainty on the spectra is only shown for the VOA 0%–5% centrality bin and is the same for all others, since all the corrections are independent of centrality. The total systematic uncertainty on the normalization, given by the quadratic sum of the uncertainty on the normalization of the pp data and the normalization of the $p\text{-Pb}$ data, amounts to 6.0% and is shown as a gray box around unity. The systematic uncertainty on $T_{p\text{Pb}}$ is shown as a light blue box around unity. For simplicity, we draw only the uncertainty for the minimum-bias value $\langle T_{p\text{Pb}} \rangle_{\text{MB}}$.

As expected, for CL1, VOM, and VOA, $Q_{p\text{Pb}}$ strongly deviates from unity at high p_T in all centrality classes, with values well above unity for central collisions and below unity for peripheral collisions. However, the spread between

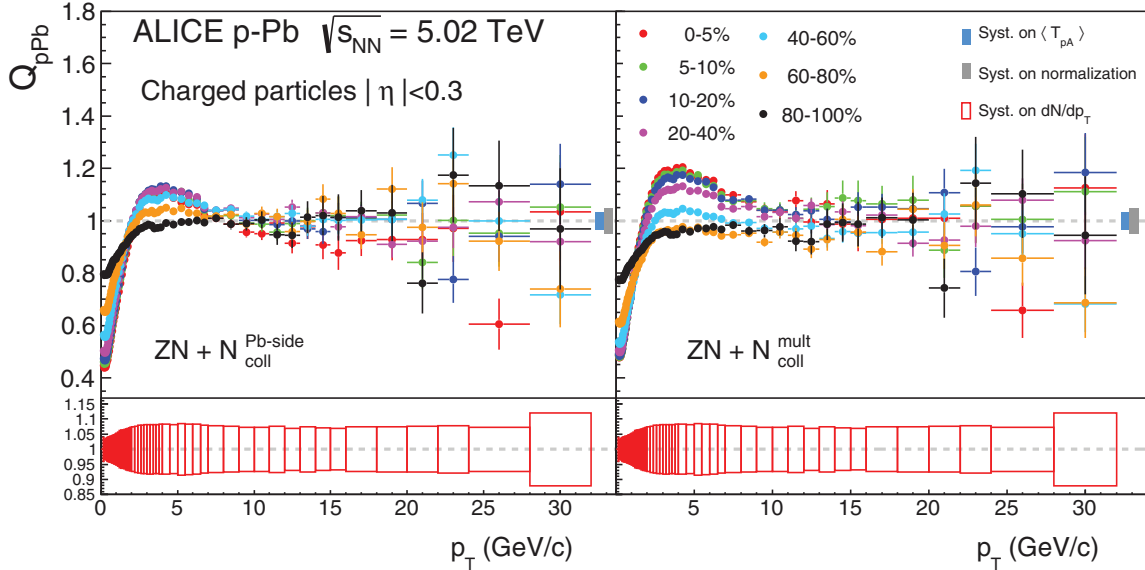


FIG. 20. (Color online) $Q_{p\text{Pb}}$ spectra with the hybrid method. Spectra are calculated in ZNA classes with $\langle N_{\text{coll}} \rangle$ as given in Table VII, and are obtained with assumptions on particle production described in Sec. VI.

centrality classes reduces with increasing rapidity gap between the range used for the centrality estimator and that used for the p_{T} measurement. There is a clear indication of the jet-veto bias in the most peripheral CL1 class, where $Q_{p\text{Pb}}$ has a significant negative slope ($p_{\text{T}} > 5 \text{ GeV}/c$) since the jet contribution to the total multiplicity increases with p_{T} . This jet-veto bias diminishes for V0M and is absent for V0A, where $Q_{p\text{Pb}} < 1$ for peripheral collisions, indicating that the multiplicity bias is still present.

In order to study the centrality determination biases further, the $Q_{p\text{Pb}}$ spectra are compared to the G-PYTHIA spectra. The event centrality is obtained from the charged-particle multiplicity in the rapidity region covered by each estimator in the same way as in data, and $\langle N_{\text{coll}} \rangle$ is directly obtained from the Monte Carlo. The calculation is shown as lines in Fig. 19. With this approach, the general trend at high p_{T} is reasonably well described for all centrality classes, particularly for CL1. This suggests that particle production at high p_{T} in $p\text{-Pb}$ collisions indeed can be approximated by an incoherent superposition of pp collisions. The agreement, however, is not as good for the V0A and V0M estimators, since the model is not adequate for forward particle production, particularly in the target fragmentation region. G-PYTHIA also reproduces the jet-veto bias, as indicated by the good agreement of the p_{T} dependence in the low- and intermediate- p_{T} region in the most peripheral CL1 collisions.

However, for central collisions, the $Q_{p\text{Pb}}$ values show a significant enhancement at intermediate $p_{\text{T}} \approx 3 \text{ GeV}/c$ (called the Cronin effect; a nuclear modification factor above unity at intermediate p_{T} , observed at lower energies in $p\text{-A}$ collisions [25,62–64]), which increases with centrality independently of the estimator used. The enhancement in the intermediate p_{T} region is about 15%, and the differences in the height of the peak among centrality estimators are small with respect to the absolute increase of the $p\text{-Pb}$ yields. The enhancement is not reproduced by our model of incoherent

superposition of pp collisions. In contrast, in the low- p_{T} region, below the Cronin peak, the yield is overestimated by the model. This overestimate at low p_{T} is expected because this p_{T} region is dominated by soft processes and therefore is not expected to scale with N_{coll} . On the other hand, the intermediate- p_{T} region is expected to be dominated by hard scatterings and should scale with N_{coll} in the absence of nuclear effects. From this we can conclude that the Cronin enhancement observed is due to nuclear modification effects, as observed in other measurements [10–13], as well as in the minimum-bias $R_{p\text{Pb}}$ [2].

The bottom right plot of Fig. 19 shows $Q_{p\text{Pb}}$ for the ZNA centrality selection. The classes selected by the ZNA present spectra much more similar to each other than the other estimators, as expected in the absence of a multiplicity bias. The height of the Cronin peak relative to the yield at high p_{T} is larger with the V0A selection, which may be seen as a sign of a remaining small bias in V0A, expected from the G-PYTHIA calculations. However, for peripheral collisions (60%–80% and 80%–100%), the absolute values of the spectra at high p_{T} indicate the presence of a bias on N_{coll} in the ZNA measurement. This is not due to the event selection but is due to the inaccurate estimate of $\langle N_{\text{coll}} \rangle$ values for peripheral events, where a small, absolute uncertainty results in a large relative deviation in the $Q_{p\text{Pb}}$ calculation.

As discussed in Sec. VI, the hybrid method uses centrality classes selected with ZNA and $\langle N_{\text{coll}} \rangle$ values determined with assumptions on particle production. Figure 20 shows the resulting $Q_{p\text{Pb}}$ values, $Q_{p\text{Pb}}^{\text{mult}}$ in the left panel and $Q_{p\text{Pb}}^{\text{Pb-side}}$ in the right panel. Here it is important to note that the ratios in the lower-right panel in Fig. 19 and in both panels in Fig. 20 have the same shape by construction and only differ due to the scaling (N_{coll}) of the reference. The small differences among the $\langle N_{\text{coll}} \rangle$ values (Table VII) are reflected in consistent $Q_{p\text{Pb}}$, which also remain consistent with unity at high p_{T} for all centrality classes. This confirms the absence

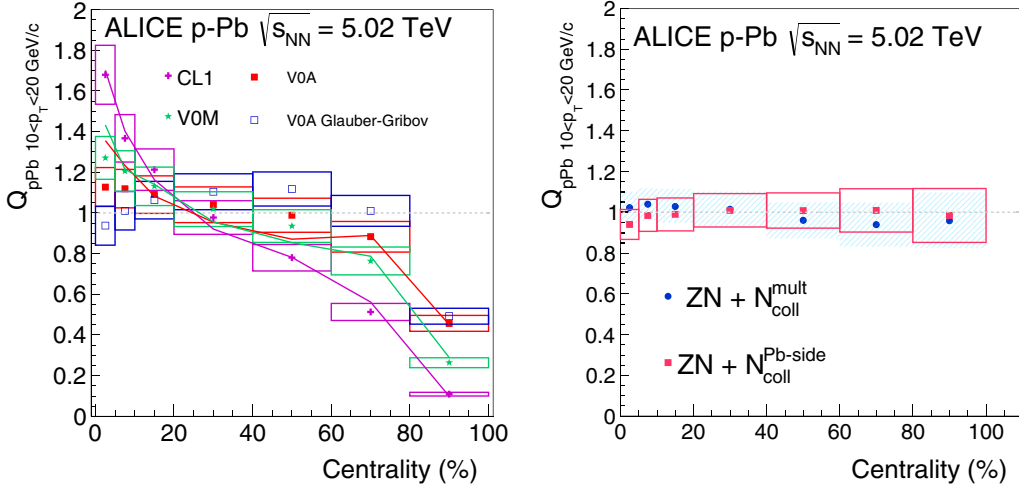


FIG. 21. (Color online) Average $Q_{p\text{Pb}}$ calculated ($10 < p_{\text{T}} < 20 \text{ GeV}/c$) as a function of centrality, with various centrality estimators. The left panel shows results from the data (points) and from the G-PYTHIA calculation (lines). The right panel shows the results for the hybrid method, where centrality classes are selected with ZNA, and $\langle N_{\text{coll}} \rangle$ are calculated with the assumptions on particle production described in Sec. VI.

of initial-state effects, already observed for minimum-bias collisions. The Cronin enhancement, which has already been noted in minimum-bias collisions, is observed to be stronger in central collisions and nearly absent in peripheral collisions. The enhancement is also weaker at 5.02 TeV compared to 200 GeV [62]. The geometry bias, described in Sec. V C, is still present and uncorrected, even with this method. Its effect is limited to peripheral classes, resulting in $Q_{p\text{Pb}} < 1$ for 80%–100%.

Figure 21 shows the mean $Q_{p\text{Pb}}$ at high momentum as a function of centrality for the various centrality estimators. The centrality dependence of $Q_{p\text{Pb}}^{\text{Glauber}}$ extracted from multiplicity distributions is shown on the left. It is reminiscent of the multiplicity bias and reproduced by the G-PYTHIA calculation

(lines in the figure). The mean $Q_{p\text{Pb}}$ changes less with increasing rapidity gap between the centrality estimator and the region where the p_{T} measurement is performed, as expected from the multiplicity bias. Instead, the $Q_{p\text{Pb}}$ extracted with the hybrid model (Fig. 21 right) is consistent with unity and the results from the two assumptions used for the $\langle N_{\text{coll}} \rangle$ calculation are in agreement.

To compare the impact of the multiplicity bias from the different estimators on the nuclear modification factors, the ratio of the spectra in pp and $p\text{-Pb}$ in different momentum ranges ($Y^{p\text{Pb}}/Y^{pp}$) is divided by the ratio of charged-particle density at midrapidity in pp and $p\text{-Pb}$ ($N_{\text{ch}}^{p\text{Pb}}/N_{\text{ch}}^{pp}$) and it is plotted as a function of $(N_{\text{ch}}^{p\text{Pb}}/N_{\text{ch}}^{pp})$ in Fig. 22. Left and middle panels show the yield at high p_{T} ($10\text{--}20 \text{ GeV}/c$) and

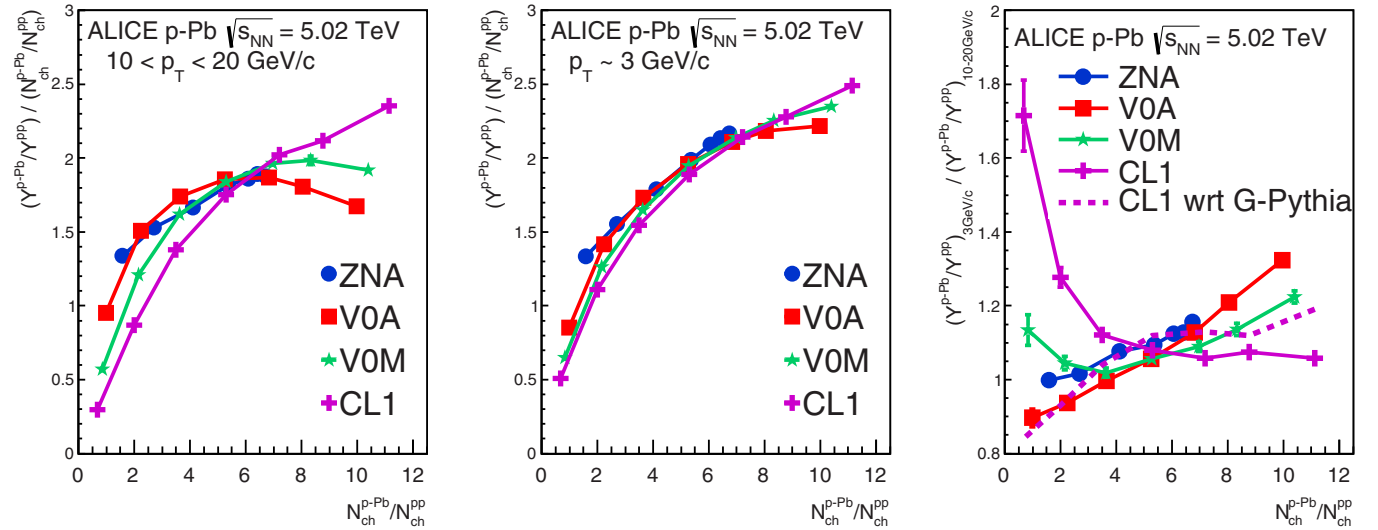


FIG. 22. (Color online) (left and middle) Ratio of yields in pp and $p\text{-Pb}$ collisions for two momentum ranges, divided by the ratio of N_{ch} in pp and $p\text{-Pb}$ collisions. (right) Ratio of the yield around $3 \text{ GeV}/c$ to the yield at high p_{T} . Values are calculated for different centrality estimators. For CL1 we also show the ratio to the value calculated with Q-PYTHIA at $3 \text{ GeV}/c$ (right panel only).

around the Cronin peak ($3 \text{ GeV}/c$), respectively. Figure 22 clearly shows the shape bias on particle spectra. Even for the same average event activity at midrapidity (corresponding to the same point on the x axis $N_{\text{ch}}^{\text{pPb}}/N_{\text{ch}}^{\text{pp}}$), the p_{T} spectra show a small but significant dependence on the centrality estimator. This is visible as a different relative number of particles ($Y^{\text{pPb}}/Y^{\text{pp}}$) in the intermediate ($3 \text{ GeV}/c$) or in the high- p_{T} ($10\text{--}20 \text{ GeV}/c$) region. Also the height of the Cronin peak relative to the high- p_{T} yield depends on the centrality estimator. This is shown in the right panel of Fig. 22, which plots the double ratio of the $p\text{-Pb}$ to pp yields at $3 \text{ GeV}/c$ and in $10\text{--}20 \text{ GeV}/c$ [$(Y^{\text{pPb}}/Y^{\text{pp}})_{3 \text{ GeV}/c}/(Y^{\text{pPb}}/Y^{\text{pp}})_{10\text{--}20 \text{ GeV}/c}$]. Since, for CL1, Q_{pPb} is not constant at high p_{T} we also plot the ratio $(Y^{\text{pPb}}/Y^{\text{pp}})_{3 \text{ GeV}/c}$ to the value calculated with G-PYTHIA at $3 \text{ GeV}/c$. The Cronin peak is clearly visible for the V0M and CL1 (with respect to G-PYTHIA) selection and is very pronounced for the V0A selection. As previously noted, the ZNA selection shows a similar trend and a value similar to that of V0A when restricted to the $dN_{\text{ch}}/d\eta$ range common to both estimators. However, the differences are still significant, and the common range is still rather small. In particular, the height of the Cronin peak is larger with ZNA than with V0A in the common $dN_{\text{ch}}/d\eta$ range, which may be seen as a sign of a remaining small bias in V0A, confirming what is observed by G-PYTHIA calculations.

The study of the correlation between observables measured in such different parts of phase space has shown that it is possible to select similar event classes by using estimators that are causally disconnected after the interaction. This is very important because this suggests that any such correlation can only arise from the initial geometry of the collision.

VIII. SUMMARY

In summary, we studied the centrality dependence of charged particle production, with measurements that comprise the charged-particle pseudorapidity density and the nuclear modification factor. The methods to determine centrality in $p\text{-A}$ collisions using multiplicity measurements or zero-degree energy are presented in detail. The former induce a bias on the hardness of the $p\text{N}$ collisions that can be quantified by the number of hard scatterings per $p\text{N}$ collision. Low-multiplicity (high-multiplicity) $p\text{-Pb}$ corresponds to lower (higher) than average number of hard scatterings. For observables based on centrality estimates from multiplicity, nuclear effects should be calculated, including this bias when comparing to an incoherent superposition of $p\text{N}$ collisions.

In contrast, the energy deposited at zero degrees by slow nucleons in the ZDC is expected to be insensitive to a multiplicity bias. Under this assumption, but in the absence of a model which properly relates the ZDC energy to the number of collisions, these are calculated assuming multiplicity scaling laws in the given kinematic ranges. In particular, we assume that the multiplicity at midrapidity is proportional to N_{part} , that multiplicity in the target-going direction is proportional to the number of wounded target nucleons, or that the yield of high- p_{T} particles is proportional to N_{coll} . The equivalence of these assumptions has been shown and discussed. Therefore, under these assumptions, we find (i) that nuclear modification

factors are consistent with unity above $\sim 8 \text{ GeV}/c$, with no centrality dependence, (ii) that the multiplicity of charged particles at midrapidity scales linearly with the total number of participants, and (iii) that the longitudinal features of $p\text{-Pb}$ collisions at $\sqrt{s_{\text{NN}}} = 5.02 \text{ TeV}$, as reflected by the centrality dependence of the pseudorapidity distributions of charged particles, are very similar to those seen in $d\text{-Au}$ collisions at RHIC energies. The latter were interpreted in support of extended longitudinal scaling in the fragmentation regions. These results represent valuable input for the study of the event activity dependence of hard probes in $p\text{-Pb}$ collision and, hence, help to establish baselines for the interpretation of the Pb-Pb data.

ACKNOWLEDGMENTS

The ALICE Collaboration would like to thank all its engineers and technicians for their invaluable contributions to the construction of the experiment and the CERN accelerator teams for the outstanding performance of the LHC complex. The ALICE Collaboration gratefully acknowledges the resources and support provided by all Grid centers and the Worldwide LHC Computing Grid (WLCG) collaboration. The ALICE Collaboration acknowledges the following funding agencies for their support in building and running the ALICE detector: the State Committee of Science, World Federation of Scientists (WFS) and the Swiss Fonds Kidagan, Armenia, the Conselho Nacional de Desenvolvimento Científico e Tecnológico (CNPq), the Financiadora de Estudos e Projetos (FINEP), the Fundação de Amparo à Pesquisa do Estado de São Paulo (FAPESP); the National Natural Science Foundation of China (NSFC), the Chinese Ministry of Education (CMOE) and the Ministry of Science and Technology of China (MSTC); the Ministry of Education and Youth of the Czech Republic; the Danish Natural Science Research Council, the Carlsberg Foundation and the Danish National Research Foundation; the European Research Council under the European Community's Seventh Framework Programme; the Helsinki Institute of Physics and the Academy of Finland; the French CNRS-IN2P3, the "Region Pays de Loire," "Region Alsace," "Region Auvergne," and the CEA, France; the German Bundesministerium für Bildung, Wissenschaft, Forschung und Technologie (BMBF) and the Helmholtz Association; the General Secretariat for Research and Technology, the Ministry of Development, Greece; the Hungarian Országos Tudományos Kutatási Alap (OTKA) and the National Office for Research and Technology (NKTH); the Department of Atomic Energy and the Department of Science and Technology of the Government of India; the Istituto Nazionale di Fisica Nucleare (INFN) and the Centro Fermi-Museo Storico della Fisica e Centro Studi e Ricerche "Enrico Fermi," Italy; a MEXT Grant-in-Aid for Specially Promoted Research, Japan; the Joint Institute for Nuclear Research, Dubna; the National Research Foundation of Korea (NRF); the Consejo Nacional de Ciencia y Tecnología (CONACYT), the Dirección General de Asuntos del Personal Académico (DGAPA), México; the Amerique Latine Formation académique-European Commission (ALFA-EC) and the EPLANET Program (European Particle Physics Latin American Network) Stichting voor Fundamenteel Onderzoek

der Materie (FOM) and the Nederlandse Organisatie voor Wetenschappelijk Onderzoek (NWO), Netherlands; the Research Council of Norway (NFR); the Polish Ministry of Science and Higher Education; the National Science Center, Poland; the Ministry of National Education/Institute for Atomic Physics and Consiliul Național al Cercetării Științifice—Executive Agency for Higher Education Research Development and Innovation Funding (CNCS-UEFISCDI)—Romania; the Ministry of Education and Science of the Russian Federation, the Russian Academy of Sciences, the Russian Federal Agency of Atomic Energy, the Russian Federal Agency for Science and Innovations, and the Russian Foundation for Basic Research; the Ministry of Education of Slovakia; the Department of Science and Technology, South Africa; the Centro de Investigaciones Energeticas, Medioam-

bientales y Tecnologicas (CIEMAT), E-Infrastructure shared between Europe and Latin America (EELA), the Ministerio de Economía y Competitividad (MINECO) of Spain, Xunta de Galicia (Conselería de Educación), the Centro de Aplicaciones Tecnológicas y Desarrollo Nuclear (CEADEN), Cubaenergía, Cuba, and the IAEA (International Atomic Energy Agency); the Swedish Research Council (VR) and the Knut & Alice Wallenberg Foundation (KAW); the Ukraine Ministry of Education and Science; the United Kingdom Science and Technology Facilities Council (STFC); the United States Department of Energy, the United States National Science Foundation, the State of Texas, the State of Ohio; the Ministry of Science, Education and Sports of Croatia and the Unity through Knowledge Fund, Croatia; and the Council of Scientific and Industrial Research (CSIR), New Delhi, India

-
- [1] C. A. Salgado, J. Alvarez-Muniz, F. Arleo, N. Armesto, M. Botje *et al.*, Proton-Nucleus collisions at the LHC: Scientific opportunities and requirements, *J. Phys. G: Nucl. Part. Phys.* **39**, 015010 (2012); arXiv:1105.3919 [hep-ph].
 - [2] B. Abelev *et al.* (ALICE Collaboration), Transverse momentum distribution and nuclear modification factor of charged particles in p -Pb collisions at 5.02 TeV, *Phys. Rev. Lett.* **110**, 082302 (2013).
 - [3] S. Chatrchyan *et al.* (CMS Collaboration), Measurement of isolated photon production in pp and PbPb collisions at $\sqrt{s_{NN}} = 2.76$ TeV, *Phys. Lett. B* **710**, 256 (2012).
 - [4] G. Aad *et al.* (ATLAS Collaboration), Measurement of Z boson Production in Pb+Pb Collisions at $\sqrt{s_{NN}} = 2.76$ TeV with the ATLAS Detector, *Phys. Rev. Lett.* **110**, 022301 (2013).
 - [5] S. Chatrchyan *et al.* (CMS Collaboration), Study of Z boson production in Pb-Pb collisions at $\sqrt{s_{NN}} = 2.76 = 2.76$ TeV, *Phys. Rev. Lett.* **106**, 212301 (2011).
 - [6] K. Aamodt *et al.* (ALICE Collaboration), Suppression of charged-particle production at large transverse momentum in central Pb-Pb collisions at $\sqrt{s_{NN}} = 2.76$ TeV, *Phys. Lett. B* **696**, 30 (2011).
 - [7] B. Abelev *et al.* (ALICE Collaboration), Measurement of charged jet suppression in Pb-Pb collisions at $\sqrt{s_{NN}} = 2.76$ TeV, *J. High Energy Phys.* **03** (2014) 013.
 - [8] B. Abelev *et al.* (ALICE Collaboration), Suppression of high transverse momentum d mesons in central Pb-Pb collisions at $\sqrt{s_{NN}} = 2.76$ TeV, *J. High Energy Phys.* **112** (2012) 1.
 - [9] B. B. Abelev *et al.* (ALICE Collaboration), J/ψ production and nuclear effects in p -Pb collisions at $\sqrt{s_{NN}} = 5.02$ TeV, *J. High Energy Phys.* **02** (2014) 073.
 - [10] B. Abelev *et al.* (ALICE Collaboration), Long-range angular correlations on the near and away side in p -Pb collisions at $\sqrt{s_{NN}} = 5.02$ TeV, *Phys. Lett. B* **719**, 29 (2013).
 - [11] B. Abelev *et al.* (ALICE Collaboration), Multiplicity dependence of the average transverse momentum in pp , p -Pb, and Pb-Pb collisions at the LHC, *Phys. Lett. B* **727**, 371 (2013).
 - [12] B. Abelev *et al.* (ALICE Collaboration), Multiplicity dependence of pion, kaon, proton and lambda production in p -Pb collisions at $\sqrt{s_{NN}} = 5.02$ TeV, *Phys. Lett. B* **728**, 25 (2014).
 - [13] B. Abelev *et al.* (ALICE Collaboration), Long-range angular correlations of π , K and p in p -Pb collisions at $\sqrt{s_{NN}} = 5.02$ TeV, *Phys. Lett. B* **726**, 164 (2013).
 - [14] K. Dusling and R. Venugopalan, Comparison of the color glass condensate to dihadron correlations in proton-proton and proton-nucleus collisions, *Phys. Rev. D* **87**, 094034 (2013).
 - [15] P. Bozek, Collective flow in p -Pb and d -Pd collisions at TeV energies, *Phys. Rev. C* **85**, 014911 (2012).
 - [16] M. Miller, K. Reygers, S. J. Sanders, and P. Steinberg, Glauber modeling in high-energy nuclear collisions, *Annu. Rev. Nucl. Part. Sci.* **57**, 205 (2007).
 - [17] B. Bialas and A. W. Czyz, Multiplicity distributions in nucleus-nucleus collisions at high energies, *Nucl. Phys. B* **111**, 461 (1976).
 - [18] A. Bialas and A. Bzdak, Wounded quarks and diquarks in high-energy collisions, *Phys. Rev. C* **77**, 034908 (2008).
 - [19] H. Pi, An Event generator for interactions between hadrons and nuclei: FRITIOF version 7.0, *Comput. Phys. Commun.* **71**, 173 (1992).
 - [20] J. Elias *et al.* (E178 Collaboration), An experimental study of multiparticle production in hadron-nucleus interactions at high energy, *Phys. Rev. D* **22**, 13 (1980).
 - [21] B. Back *et al.* (PHOBOS Collaboration), Scaling of charged particle production in $d + \text{Au}$ collisions at $s(NN)^{**}(1/2) = 200$ GeV, *Phys. Rev. C* **72**, 031901 (2005).
 - [22] A. Adare *et al.* (PHENIX Collaboration), Centrality categorization for $R_{p(d)+A}$ in high-energy collisions, *Phys. Rev. C* **90**, 034902 (2014).
 - [23] J. Adams *et al.* (STAR Collaboration), Evidence from $d + \text{Au}$ measurements for final-state suppression of high- $p(T)$ hadrons in $\text{Au} + \text{Au}$ collisions at RHIC, *Phys. Rev. Lett.* **91**, 072304 (2003).
 - [24] B. Abelev *et al.* (ALICE Collaboration), Pseudorapidity density of charged particles in p -Pb collisions at 5.02 TeV, *Phys. Rev. Lett.* **110**, 032301 (2013).
 - [25] J. Adams *et al.* (STAR Collaboration), Pion, kaon, proton and anti-proton transverse momentum distributions from $p+p$ and $d+\text{Au}$ collisions at $\sqrt{s_{NN}} = 200$ GeV, *Phys. Lett. B* **616**, 8 (2005).
 - [26] F. Sikler, Centrality control of hadron nucleus interactions by detection of slow nucleons, arXiv:hep-ph/0304065 [hep-ph].
 - [27] B. Alessandro *et al.* (ALICE Collaboration), Physics performance report II, *J. Phys. G* **32**, 1295 (2006).
 - [28] V. Gribov, Glauber corrections and the interaction between high-energy hadrons and nuclei, *Sov. Phys. JETP* **29**, 483 (1969).

- [29] X.-N. Wang and M. Gyulassy, Hijing: A Monte Carlo model for multiple jet production in pp, pA, and AA collisions, *Phys. Rev. D* **44**, 3501 (1991).
- [30] K. Aamodt *et al.* (ALICE Collaboration), The ALICE experiment at the CERN LHC, *J. Instrum.* **3**, S08002 (2008).
- [31] B. B. Abelev *et al.* (ALICE Collaboration), Performance of the ALICE Experiment at the CERN LHC, *Int. J. Mod. Phys. A* **29**, 1430044 (2014).
- [32] B. B. Abelev *et al.* (ALICE Collaboration), Measurement of visible cross sections in proton-lead collisions at $\sqrt{s_{NN}} = 5.02$ TeV in van der Meer scans with the ALICE detector, *J. Instrum.* **9** (2014) 1100.
- [33] R. Glauber, in *Lectures in Theoretical Physics*, edited by W. E. Brittin and L. G. Dunham (1959), Vol. 1, p. 315.
- [34] R. Glauber, Cross sections in deuterium at high energies, *Phys. Rev.* **100**, 242 (1955).
- [35] R. Glauber, Quantum optics and heavy-ion physics, *Nucl. Phys. A* **774**, 3 (2006).
- [36] A. P. T. W. Ludlam and A. Shor, Hijet. A Monte Carlo event generator for p -nucleus and nucleus-nucleus collisions, BNL **37196**, 373 (1985).
- [37] A. Shor and R. Longacre, Effects of secondary interactions in proton-nucleus and nucleus-nucleus collisions using the hijet event generator, *Phys. Lett. B* **218**, 100 (1989).
- [38] B. Abelev *et al.* (ALICE Collaboration), Centrality determination of Pb-Pb collisions at $\sqrt{s_{NN}} = 2.76$ TeV with ALICE, *Phys. Rev. C* **88**, 044909 (2013).
- [39] H. De Vries, C. W. De Jager, and C. De Vries, Nuclear charge and magnetization density distribution parameters from elastic electron scattering, *At. Data Nucl. Data Tables* **36**, 495 (1987).
- [40] K. Nakamura *et al.* (Particle Data Group Collaboration), Review of particle physics, *J. Phys. G* **37**, 075021 (2010).
- [41] B. Abelev *et al.* (ALICE Collaboration), Measurement of inelastic, single- and double-diffraction cross sections in proton-proton collisions at the LHC with ALICE, *Eur. Phys. J. C* **73**, 2456 (2013).
- [42] B. B. Heiselberg, G. Baym, L. Frankfurt, and M. Strikman, Color transparency, color opacity and fluctuations in nuclear collisions, *Phys. Rev. Lett.* **67**, 2946 (1991).
- [43] V. Guzey and M. Strikman, Proton-nucleus scattering and cross-section fluctuations at RHIC and LHC, *Phys. Lett. B* **633**, 245 (2006).
- [44] M. Alvioli and M. Strikman, Color fluctuation effects in proton-nucleus collisions, *Phys. Lett. B* **722**, 347 (2013).
- [45] G. Aad *et al.* (ATLAS Collaboration), Measurement of the charged particle multiplicity distribution in p +Pb collision at $\sqrt{s_{NN}} = 5$ TeV with the ATLAS detector at LHC, *ATLAS-CONF-2013-096* (2013).
- [46] C. Loizides, J. Nagle, and P. Steinberg, Improved version of the PHOBOS Glauber Monte Carlo, [arXiv:1408.2549](https://arxiv.org/abs/1408.2549) [nucl-ex].
- [47] I. Chemakin *et al.* (E910 Collaboration), Measuring centrality with slow protons in proton nucleus collisions at the AGS, *Phys. Rev. C* **60**, 024902 (1999).
- [48] A. Letourneau *et al.*, Composite particle emission in the reaction $p + \text{Au}$ at 2.5 GeV, *Nucl. Phys. A* **712**, 133 (2002).
- [49] A. Kowalczyk, Proton-induced spallation reactions in the energy range 0.1–10 GeV, [arXiv:0801.0700](https://arxiv.org/abs/0801.0700) [nucl-th].
- [50] A. Dabrowska *et al.* (KLM Collaboration), Particle production in interactions of 200-GeV/nucleon oxygen and sulfur nuclei in nuclear emulsion, *Phys. Rev. D* **47**, 1751 (1993).
- [51] R. Brun *et al.*, GEANT detector description and simulation tool, CERN Program Library Long Writeup W5013, 1–467 (1994).
- [52] S. Roesler, R. Engel, and J. Ranft, The Monte Carlo event generator DPMJET-III, [arXiv:hep-ph/0012252](https://arxiv.org/abs/hep-ph/0012252).
- [53] A. Giovannini and L. V. Hove, Negative binomial multiplicity distributions in high-energy hadron collisions, *Z. Phys. C: Part. Fields* **30**, 391 (1986).
- [54] T. Sjostrand, S. Mrenna, and P. Z. Skands, PYTHIA 6.4 Physics and Manual, *J. High Energy Phys.* **05** (2006) 026.
- [55] J. Jia, Influence of the nucleon-nucleon collision geometry on the determination of the nuclear modification factor for nucleon-nucleus and nucleus-nucleus collisions, *Phys. Lett. B* **681**, 320 (2009).
- [56] R. Xu, W.-T. Deng, and X.-N. Wang, Nuclear modification of high- p_T hadron spectra in $p + A$ collisions at LHC, *Phys. Rev. C* **86**, 051901 (2012).
- [57] A. Dumitru, D. E. Kharzeev, E. M. Levin, and Y. Nara, Gluon Saturation in pA Collisions at the LHC: KLN Model Predictions For Hadron Multiplicities, *Phys. Rev. C* **85**, 044920 (2012).
- [58] P. Tribedy and R. Venugopalan, QCD saturation at the LHC: comparisons of models to $p + p$ and $A + A$ data and predictions for $p + \text{Pb}$ collisions, *Phys. Lett. B* **710**, 125 (2012).
- [59] J. L. Albacete, A. Dumitru, H. Fujii, and Y. Nara, CGC predictions for $p + \text{Pb}$ collisions at the LHC, *Nucl. Phys. A* **897**, 1 (2013).
- [60] B. B. Abelev *et al.* (ALICE Collaboration), Transverse momentum dependence of inclusive primary charged-particle production in p -Pb collisions at $\sqrt{s_{NN}} = 5.02$ TeV, *Eur. Phys. J. C* **74**, 3054 (2014).
- [61] B. B. Abelev *et al.* (ALICE Collaboration), Energy Dependence of the Transverse Momentum Distributions of Charged Particles in pp Collisions Measured by ALICE, *Eur. Phys. J. C* **73**, 2662 (2013).
- [62] J. W. Cronin, H. J. Frisch, M. J. Shochet, J. P. Boymond, P. A. Piroué, and R. L. Sumner, Production of hadrons at large transverse momentum at 200, 300, and 400 GeV, *Phys. Rev. D* **11**, 3105 (1975).
- [63] S. S. Adler *et al.* (PHENIX Collaboration), Absence of suppression in particle production at large transverse momentum in $\sqrt{s_{NN}} = 200$ GeV $d + \text{Au}$ collisions, *Phys. Rev. Lett.* **91**, 072303 (2003).
- [64] A. Accardi, Cronin effect in proton-nucleus collisions: A Survey of theoretical models, [arXiv:hep-ph/0212148](https://arxiv.org/abs/hep-ph/0212148).

- S. Altinpinar,¹⁸ I. Altsybeev,¹²⁹ C. Alves Garcia Prado,¹¹⁸ C. Andrei,⁷⁷ A. Andronic,⁹⁶ V. Anguelov,⁹² J. Anielski,⁵³ T. Antićić,⁹⁷ F. Antinori,¹⁰⁷ P. Antonioli,¹⁰⁴ L. Aphacetche,¹¹² H. Appelhäuser,⁵² S. Arcelli,²⁸ N. Armesto,¹⁷ R. Arnaldi,¹¹⁰ T. Aronsson,¹³⁴ I. C. Arsene,²² M. Arslanok,⁵² A. Augustinus,³⁶ R. Averbeck,⁹⁶ M. D. Azmi,¹⁹ M. Bach,⁴² A. Badalà,¹⁰⁶ Y. W. Baek,^{69,43} S. Bagnasco,¹¹⁰ R. Bailhache,⁵² R. Bala,⁸⁹ A. Baldissari,¹⁵ M. Ball,⁹¹ F. Baltasar Dos Santos Pedrosa,³⁶ R. C. Baral,⁶⁰ A. M. Barbano,¹¹⁰ R. Barbera,²⁹ F. Barile,³³ G. G. Barnaföldi,¹³³ L. S. Barnby,¹⁰¹ V. Barret,⁶⁹ P. Bartalini,⁷ J. Bartke,¹¹⁵ E. Bartsch,⁵² M. Basile,²⁸ N. Bastid,⁶⁹ S. Basu,¹³⁰ B. Bathen,⁵³ G. Batigne,¹¹² A. Batista Camejo,⁶⁹ B. Batyunya,⁶⁵ P. C. Batzing,²² I. G. Bearden,⁷⁹ H. Beck,⁵² C. Bedda,⁹³ N. K. Behera,⁴⁷ I. Belikov,⁵⁴ F. Bellini,²⁸ H. Bello Martinez,² R. Bellwied,¹²⁰ R. Belmont,¹³² E. Belmont-Moreno,⁶³ V. Belyaev,⁷⁵ G. Bencedi,¹³³ S. Beole,²⁷ I. Berceanu,⁷⁷ A. Bercuci,⁷⁷ Y. Berdnikov,⁸⁴ D. Berenyi,¹³³ R. A. Bertens,⁵⁶ D. Berzana,³⁶ L. Betev,³⁶ A. Bhasin,⁸⁹ I. R. Bhat,⁸⁹ A. K. Bhati,⁸⁶ B. Bhattacharjee,⁴⁴ J. Bhom,¹²⁶ L. Bianchi,^{120,27} N. Bianchi,⁷¹ C. Bianchin,⁵⁶ J. Bielčík,³⁹ J. Bielčíková,⁸² A. Bilandzic,⁷⁹ S. Biswas,⁷⁸ S. Bjelogrlic,⁵⁶ F. Blanco,¹⁰ D. Blau,⁹⁹ C. Blume,⁵² F. Bock,^{73,92} A. Bogdanov,⁷⁵ H. Bøggild,⁷⁹ L. Boldizsár,¹³³ M. Bombara,⁴⁰ J. Book,⁵² H. Borel,¹⁵ A. Borissov,⁹⁵ M. Borri,⁸¹ F. Bossú,⁶⁴ M. Botje,⁸⁰ E. Botta,²⁷ S. Böttger,⁵¹ P. Braun-Munzinger,⁹⁶ M. Bregant,¹¹⁸ T. Breitner,⁵¹ T. A. Broker,⁵² T. A. Browning,⁹⁴ M. Broz,³⁹ E. Bruna,¹¹⁰ G. E. Bruno,³³ D. Budnikov,⁹⁸ H. Buesching,⁵² S. Bufalino,^{36,110} P. Buncic,³⁶ O. Busch,⁹² Z. Buthelezi,⁶⁴ J. T. Buxton,²⁰ D. Caffarri,^{30,36} X. Cai,⁷ H. Caines,¹³⁴ L. Calero Diaz,⁷¹ A. Caliva,⁵⁶ E. Calvo Villar,¹⁰² P. Camerini,²⁶ F. Carena,³⁶ W. Carena,³⁶ J. Castillo Castellanos,¹⁵ A. J. Castro,¹²³ E. A. R. Casula,²⁵ V. Catanescu,⁷⁷ C. Cavicchioli,³⁶ C. Ceballos Sanchez,⁹ J. Cepila,³⁹ P. Cerello,¹¹⁰ B. Chang,¹²¹ S. Chapeland,³⁶ M. Chartier,¹²² J. L. Charvet,¹⁵ S. Chattopadhyay,¹³⁰ S. Chattopadhyay,¹⁰⁰ V. Chelnokov,³ M. Cherney,⁸⁵ C. Cheshkov,¹²⁸ B. Cheynis,¹²⁸ V. Chibante Barroso,³⁶ D. D. Chinellato,¹¹⁹ P. Chochula,³⁶ K. Choi,⁹⁵ M. Chojnacki,⁷⁹ S. Choudhury,¹³⁰ P. Christakoglou,⁸⁰ C. H. Christensen,⁷⁹ P. Christiansen,³⁴ T. Chujo,¹²⁶ S. U. Chung,⁹⁵ C. Cicalo,¹⁰⁵ L. Cifarelli,^{12,28} F. Cindolo,¹⁰⁴ J. Cleymans,⁸⁸ F. Colamaria,³³ D. Colella,³³ A. Collu,²⁵ M. Colocci,²⁸ G. Conesa Balbastre,⁷⁰ Z. Conesa del Valle,⁵⁰ M. E. Connors,¹³⁴ J.G. Contreras,^{11,39} T. M. Cormier,⁸³ Y. Corrales Morales,²⁷ I. Cortés Maldonado,² P. Cortese,³² M. R. Cosentino,¹¹⁸ F. Costa,³⁶ P. Crochet,⁶⁹ R. Cruz Albino,¹¹ E. Cuautle,⁶² L. Cunqueiro,³⁶ T. Dahms,⁹¹ A. Dainese,¹⁰⁷ A. Danu,⁶¹ D. Das,¹⁰⁰ I. Das,⁵⁰ S. Das,⁴ A. Dash,¹¹⁹ S. Dash,⁴⁷ S. De,^{118,130} A. De Caro,^{31,12} G. de Cataldo,¹⁰³ J. de Cuveland,⁴² A. De Falco,²⁵ D. De Gruttola,^{31,12} N. De Marco,¹¹⁰ S. De Pasquale,³¹ A. Deloff,⁷⁶ E. Dénes,¹³³ G. D'Erasmo,³³ D. Di Bari,³³ A. Di Mauro,³⁶ P. Di Nezza,⁷¹ M. A. Diaz Corchero,¹⁰ T. Dietel,⁸⁸ P. Dillenseger,⁵² R. Divià,³⁶ Ø. Djupsland,¹⁸ A. Dobrin,⁵⁶ T. Dobrowolski,⁷⁶ D. Domenicis Gimenez,¹¹⁸ B. Dönigus,⁵² O. Dordic,²² A. K. Dubey,¹³⁰ A. Dubla,⁵⁶ L. Ducroux,¹²⁸ P. Dupieux,⁶⁹ A. K. Dutta Majumdar,¹⁰⁰ R. J. Ehlers,¹⁰³ D. Elia,¹⁰³ H. Engel,⁵¹ B. Erazmus,^{112,36} H. A. Erdal,³⁷ D. Eschweiler,⁴² B. Espagnon,⁵⁰ M. Esposito,³⁶ M. Estienne,¹¹² S. Esumi,¹²⁶ D. Evans,¹⁰¹ S. Evdokimov,¹¹¹ G. Eyyubova,³⁹ L. Fabbietti,⁹¹ D. Fabris,¹⁰⁷ J. Faivre,⁷⁰ A. Fantoni,⁷¹ M. Fasel,⁷³ L. Feldkamp,⁵³ D. Felea,⁶¹ A. Feliciello,¹¹⁰ G. Feofilov,¹²⁹ J. Ferencei,⁸² A. Fernández Téllez,² E. G. Ferreiro,¹⁷ A. Ferretti,²⁷ A. Festanti,³⁰ J. Figiel,¹¹⁵ M. A. S. Figueredo,¹²² S. Filchagin,⁹⁸ D. Finogeev,⁵⁵ F. M. Fionda,¹⁰³ E. M. Fiore,³³ M. Floris,³⁶ S. Foertsch,⁶⁴ P. Foka,⁹⁶ S. Fokin,⁹⁹ E. Fragiocomo,¹⁰⁹ A. Francescon,^{36,30} U. Frankenfeld,⁹⁶ U. Fuchs,³⁶ C. Furget,⁷⁰ A. Furs,⁵⁵ M. Fusco Girard,³¹ J. J. Gaardhøje,⁷⁹ M. Gagliardi,²⁷ A. M. Gago,¹⁰² M. Gallio,²⁷ D. R. Gangadharan,⁷³ P. Ganoti,⁸⁷ C. Gao,⁷ C. Garabatos,⁹⁶ E. Garcia-Solis,¹³ C. Gargiulo,³⁶ P. Gasik,⁹¹ M. Germain,¹¹² A. Gheata,³⁶ M. Gheata,^{36,61} B. Ghidini,³³ P. Ghosh,¹³⁰ S. K. Ghosh,⁴ P. Gianotti,⁷¹ P. Giubellino,³⁶ P. Giubilato,³⁰ E. Gladysz-Dziadus,¹¹⁵ P. Glässel,⁹² A. Gomez Ramirez,⁵¹ P. González-Zamora,¹⁰ S. Gorbunov,⁴² L. Görlich,¹¹⁵ S. Gotovac,¹¹⁴ V. Grabski,⁶³ L. K. Graczykowski,¹³¹ A. Grelli,⁵⁶ A. Grigoras,³⁶ C. Grigoras,³⁶ V. Grigoriev,⁷⁵ A. Grigoryan,¹ S. Grigoryan,⁶⁵ B. Grinyov,³ N. Grion,¹⁰⁹ J. Gronefeld,⁹⁶ J. F. Grosse-Oetringhaus,³⁶ R. Grossi,³⁶ J.-Y. Grossiord,¹²⁷ F. Guber,⁵⁵ R. Guernane,⁷⁰ B. Guerzoni,²⁸ K. Gulbrandsen,⁷⁹ H. Gulkanyan,¹ T. Gunji,¹²⁵ A. Gupta,⁸⁹ R. Gupta,⁸⁹ R. Haake,⁵³ Ø. Haaland,¹⁸ C. Hadjidakis,⁵⁰ M. Haiduc,⁶¹ H. Hamagaki,¹²⁵ G. Hamar,¹³³ L. D. Hanratty,¹⁰¹ A. Hansen,⁷⁹ J. W. Harris,¹³⁴ H. Hartmann,⁴² A. Harton,¹³ D. Hatzifotiadou,¹⁰⁴ S. Hayashi,¹²⁵ S. T. Heckel,⁵² M. Heide,⁵³ H. Helstrup,³⁷ A. Hergelegui,⁷⁷ G. Herrera Corral,¹¹ B. A. Hess,³⁵ K. F. Hetland,³⁷ T. E. Hilden,⁴⁵ H. Hillemanns,³⁶ B. Hippolyte,⁵⁴ P. Hristov,³⁶ M. Huang,¹⁸ T. J. Humanic,²⁰ N. Hussain,⁴⁴ T. Hussain,¹⁹ D. Hutter,⁴² D. S. Hwang,²¹ R. Ilkaev,⁹⁸ I. Ilkiv,⁷⁶ M. Inaba,¹²⁶ G. M. Innocenti,²⁷ C. Ionita,³⁶ M. Ippolitov,^{75,99} M. Irfan,¹⁹ M. Ivanov,⁹⁶ V. Ivanov,⁸⁴ A. Jachotkowski,²⁹ P. M. Jacobs,⁷³ C. Jahnke,¹¹⁸ H. J. Jang,⁶⁷ M. A. Janik,¹³¹ P. H. S. Y. Jayarathna,¹²⁰ C. Jena,³⁰ S. Jena,¹²⁰ R. T. Jimenez Bustamante,⁶² P. G. Jones,¹⁰¹ H. Jung,⁴³ A. Jusko,¹⁰¹ V. Kadyshevskiy,⁶⁵ P. Kalinak,⁵⁸ A. Kalweit,³⁶ J. Kamin,⁵² J. H. Kang,¹³⁵ V. Kaplin,⁷⁵ S. Kar,¹³⁰ A. Karasu Uysal,⁶⁸ O. Karavichev,⁵⁵ T. Karavicheva,⁵⁵ E. Karpechev,⁵⁵ U. Kebschull,⁵¹ R. Keidel,¹³⁶ D. L. D. Keijdener,⁵⁶ M. Keil,³⁶ B. Ketzer,⁹¹ K. H. Khan,¹⁶ M. M. Khan,¹⁹ P. Khan,¹⁰⁰ S. A. Khan,¹³⁰ A. Khanzadeev,⁸⁴ Y. Kharlov,¹¹¹ B. Kileng,³⁷ B. Kim,¹³⁵ D. W. Kim,^{67,43} D. J. Kim,¹²¹ H. Kim,¹³⁵ J. S. Kim,⁴³ M. Kim,⁴³ M. Kim,¹³⁵ S. Kim,²¹ T. Kim,¹³⁵ S. Kirsch,⁴² I. Kisel,⁴² S. Kiselev,⁵⁷ A. Kisiel,¹³¹ G. Kiss,¹³³ J. L. Klay,⁶ C. Klein,⁵² J. Klein,⁹² C. Klein-Bösing,⁵³ A. Kluge,³⁶ M. L. Knichel,⁹² A. G. Knospe,¹¹⁶ T. Kobayashi,¹²⁶ C. Kobdaj,¹¹³ M. Kofarago,³⁶ M. K. Köhler,⁹⁶ T. Kollegger,^{42,96} A. Kolojvari,¹²⁹ V. Kondratiev,¹²⁹ N. Kondratyeva,⁷⁵ E. Kondratyuk,¹¹¹ A. Konevskikh,⁵⁵ V. Kovalenko,¹²⁹ M. Kowalski,^{115,36} S. Kox,⁷⁰ G. Koyithatta Meethaleveedu,⁴⁷ J. Kral,¹²¹ I. Králík,⁵⁸ A. Kravčáková,⁴⁰ M. Krelina,³⁹ M. Kretz,⁴² M. Krivda,^{58,101} F. Krizek,⁸² E. Kryshen,³⁶ M. Krzewicki,^{96,42} A. M. Kubera,²⁰ V. Kućera,⁸² Y. Kucherlaev,^{99,*} T. Kugathasan,³⁶ C. Kuhn,⁵⁴ P. G. Kuijer,⁸⁰ I. Kulakov,⁴² J. Kumar,⁴⁷ P. Kurashvili,⁷⁶ A. Kurepin,⁵⁵ A. B. Kurepin,⁵⁵ A. Kuryakin,⁹⁸ S. Kushpil,⁸² M. J. Kweon,⁴⁹ Y. Kwon,¹³⁵ S. L. La Pointe,¹¹⁰ P. La Rocca,²⁹ C. Lagana Fernandes,¹¹⁸ I. Lakomov,^{36,50} R. Langoy,⁴¹ C. Lara,⁵¹ A. Lardeux,¹⁵ A. Lattuca,²⁷ E. Laudi,³⁶ R. Lea,²⁶ L. Leardini,⁹² G. R. Lee,¹⁰¹ I. Legrand,³⁶ J. Lehnert,⁵² R. C. Lemmon,⁸¹ V. Lenti,¹⁰³ E. Leogrande,⁵⁶ I. León Monzón,¹¹⁷ M. Leoncino,²⁷ P. Lévai,¹³³ S. Li,^{7,69} X. Li,¹⁴ J. Lien,⁴¹

- R. Lietava,¹⁰¹ S. Lindal,²² V. Lindenstruth,⁴² C. Lippmann,⁹⁶ M. A. Lisa,²⁰ H. M. Ljunggren,³⁴ D. F. Lodato,⁵⁶ P. I. Loenne,¹⁸ V. R. Loggins,¹³² V. Loginov,⁷⁵ D. Lohner,⁹² C. Loizides,⁷³ K. Lokesh,^{78,86} X. Lopez,⁶⁹ E. López Torres,⁹ A. Lowe,¹³³ X.-G. Lu,⁹² P. Luettig,⁵² M. Lunardon,³⁰ G. Luparello,^{26,56} A. Maevskaia,⁵⁵ M. Mager,³⁶ S. Mahajan,⁸⁹ S. M. Mahmood,²² A. Maire,⁵⁴ R. D. Majka,¹³⁴ M. Malaev,⁸⁴ I. Maldonado Cervantes,⁶² L. Malinina,^{65,†} D. Mal'Kevich,⁵⁷ P. Malzacher,⁹⁶ A. Mamontov,⁹⁸ L. Manceau,¹¹⁰ V. Manko,⁹⁹ F. Manso,⁶⁹ V. Manzari,^{36,103} M. Marchisone,²⁷ J. Mareš,⁵⁹ G. V. Margagliotti,²⁶ A. Margotti,¹⁰⁴ J. Margutti,⁵⁶ A. Marín,⁹⁶ C. Markert,^{116,36} M. Marquardt,⁵² I. Martashvili,¹²³ N. A. Martin,⁹⁶ J. Martin Blanco,¹¹² P. Martinengo,³⁶ M. I. Martínez,² G. Martínez García,¹¹² Y. Martynov,³ A. Mas,¹¹⁸ S. Masciocchi,⁹⁶ M. Masera,²⁷ A. Masoni,¹⁰⁵ L. Massacrier,¹¹² A. Mastroserio,³³ A. Matyja,¹¹⁵ C. Mayer,¹¹⁵ J. Mazer,¹²³ M. A. Mazzoni,¹⁰⁸ D. McDonald,¹²⁰ F. Meddi,²⁴ A. Menchaca-Rocha,⁶³ E. Meninno,³¹ J. Mercado Pérez,⁹² M. Meres,³⁸ Y. Miake,¹²⁶ M. M. Mieskolainen,⁴⁵ K. Mikhaylov,^{57,65} L. Milano,³⁶ J. Milosevic,^{22,‡} L. M. Minervini,^{103,23} A. Mischke,⁵⁶ A. N. Mishra,⁴⁸ D. Miśkowiec,⁹⁶ J. Mitra,¹³⁰ C. M. Mitu,⁶¹ J. Mlynarz,¹³² N. Mohammadi,⁵⁶ B. Mohanty,^{130,78} L. Molnar,⁵⁴ L. Montaño Zetina,¹¹ E. Montes,¹⁰ M. Morando,³⁰ D. A. Moreira De Godoy,¹¹² S. Moretto,³⁰ A. Morreale,¹¹² A. Morsch,³⁶ V. Muccifora,⁷¹ E. Mudnic,¹¹⁴ D. Mühlheim,⁵³ S. Muhuri,¹³⁰ M. Mukherjee,¹³⁰ H. Müller,³⁶ M. G. Munhoz,¹¹⁸ S. Murray,⁶⁴ L. Musa,³⁶ J. Musinsky,⁵⁸ B. K. Nandi,⁴⁷ R. Nania,¹⁰⁴ E. Nappi,¹⁰³ M. U. Naru,¹⁶ C. Nattrass,¹²³ K. Nayak,⁷⁸ T. K. Nayak,¹³⁰ S. Nazarenko,⁹⁸ A. Nedosekin,⁵⁷ L. Nellen,⁶² F. Ng,¹²⁰ M. Nicassio,⁹⁶ M. Niculescu,^{61,36} J. Niedziela,³⁶ B. S. Nielsen,⁷⁹ S. Nikolaev,⁹⁹ S. Nikulin,⁹⁹ V. Nikulin,⁸⁴ B. S. Nilsen,⁸⁵ F. Noferini,^{12,104} P. Nomokonov,⁶⁵ G. Nooren,⁵⁶ J. Norman,¹²² A. Nyandin,⁹⁹ J. Nystrand,¹⁸ H. Oeschler,⁹² S. Oh,¹³⁴ S. K. Oh,^{66,§} A. Okatan,⁶⁸ T. Okubo,⁴⁶ L. Olah,¹³³ J. Oleniacz,¹³¹ A. C. Oliveira Da Silva,¹¹⁸ J. Onderwaater,⁹⁶ C. Oppedisano,¹¹⁰ A. Ortiz Velasquez,^{34,62} A. Oskarsson,³⁴ J. Otwinowski,^{96,115} K. Oyama,⁹² M. Ozdemir,⁵² Y. Pachmayer,⁹² P. Pagano,³¹ G. Paić,⁶² C. Pajares,¹⁷ S. K. Pal,¹³⁰ D. Pant,⁴⁷ V. Papikyan,¹ G. S. Pappalardo,¹⁰⁶ P. Pareek,⁴⁸ W. J. Park,⁹⁶ S. Parmar,⁸⁶ A. Passfeld,⁵³ D. I. Patalakha,¹¹¹ V. Paticchio,¹⁰³ B. Paul,¹⁰⁰ T. Pawlak,¹³¹ T. Peitzmann,⁵⁶ H. Pereira Da Costa,¹⁵ E. Pereira De Oliveira Filho,¹¹⁸ D. Peresunko,^{99,75} C. E. Pérez Lara,⁸⁰ V. Peskov,⁵² Y. Pestov,⁵ V. Petráček,³⁹ M. Petris,⁷⁷ V. Petrov,¹¹¹ M. Petrovici,⁷⁷ C. Petta,²⁹ S. Piano,¹⁰⁹ M. Pikna,³⁸ P. Pillot,¹¹² O. Pinazza,^{36,104} L. Pinsky,¹²⁰ D. B. Piyarathna,¹²⁰ M. Płoskoń,⁷³ M. Planinic,¹²⁷ J. Pluta,¹³¹ S. Pochybova,¹³³ P. L. M. Podesta-Lerma,¹¹⁷ M. G. Poghosyan,⁸⁵ E. H. O. Pohjoisaho,⁴⁵ B. Polichtchouk,¹¹¹ N. Poljak,¹²⁷ W. Poonsawat,¹¹³ A. Pop,⁷⁷ S. Porteboeuf-Houssais,⁶⁹ J. Porter,⁷³ J. Pospisil,⁸² S. K. Prasad,⁴ R. Preghenella,^{104,36,12} F. Prino,¹¹⁰ C. A. Pruneau,¹³² I. Pshenichnov,⁵⁵ M. Puccio,¹¹⁰ G. Puddu,²⁵ P. Pujahari,¹³² V. Punin,⁹⁸ J. Putschke,¹³² H. Qvigstad,²² A. Rachevski,¹⁰⁹ S. Raha,⁴ S. Rajput,⁸⁹ J. Rak,¹²¹ A. Rakotozafindrabe,¹⁵ L. Ramello,³² R. Raniwala,⁹⁰ S. Raniwala,⁹⁰ S. S. Räsänen,⁴⁵ B. T. Rascanu,⁵² D. Rathee,⁸⁶ A. W. Rauf,¹⁶ V. Razazi,²⁵ K. F. Read,¹²³ J. S. Real,⁷⁰ K. Redlich,^{76,||} R. J. Reed,^{134,132} A. Rehman,¹⁸ P. Reichelt,⁵² M. Reicher,⁵⁶ F. Reidt,^{36,92} R. Renfordt,⁵² A. R. Reolon,⁷¹ A. Reshetin,⁵⁵ F. Rettig,⁴² J.-P. Revol,³⁵ K. Reygers,⁹² V. Riabov,⁸⁴ R. A. Ricci,⁷² T. Richert,³⁴ M. Richter,²² P. Riedler,³⁶ W. Riegler,³⁶ F. Riggi,²⁹ C. Ristea,⁶¹ A. Rivetti,¹¹⁰ E. Rocco,⁵⁶ M. Rodríguez Cahuantzi,^{2,11} A. Rodriguez Manso,⁸⁰ K. Røed,²² E. Rogochaya,⁶⁵ S. Rohni,⁸⁹ D. Rohr,⁴² D. Röhrich,¹⁸ R. Romita,¹²² F. Ronchetti,⁷¹ L. Ronflette,¹¹² P. Rosnet,⁶⁹ A. Rossi,³⁶ F. Roukoutakis,⁸⁷ A. Roy,⁴⁸ C. Roy,⁵⁴ P. Roy,¹⁰⁰ A. J. Rubio Montero,¹⁰ R. Rui,²⁶ R. Russo,²⁷ E. Ryabinkin,⁹⁹ Y. Ryabov,⁸⁴ A. Rybicki,¹¹⁵ S. Sadovsky,¹¹¹ K. Šafařík,³⁶ B. Sahlmuller,⁵² P. Sahoo,⁴⁸ R. Sahoo,⁴⁸ S. Sahoo,⁶⁰ P. K. Sahu,⁶⁰ J. Saini,¹³⁰ S. Sakai,⁷¹ C. A. Salgado,¹⁷ J. Salzwedel,²⁰ S. Sambyal,⁸⁹ V. Samsonov,⁸⁴ X. Sanchez Castro,⁵⁴ L. Šándor,⁵⁸ A. Sandoval,⁶³ M. Sano,¹²⁶ G. Santagati,²⁹ D. Sarkar,¹³⁰ E. Scapparone,¹⁰⁴ F. Scarlassara,³⁰ R. P. Scharenberg,⁹⁴ C. Schiaua,⁷⁷ R. Schicker,⁹² C. Schmidt,⁹⁶ H. R. Schmidt,³⁵ S. Schuchmann,⁵² J. Schukraft,³⁶ M. Schulc,³⁹ T. Schuster,¹³⁴ Y. Schutz,^{112,36} K. Schwarz,⁹⁶ K. Schweda,⁹⁶ G. Scioli,²⁸ E. Scomparin,¹¹⁰ R. Scott,¹²³ K. S. Seeder,¹¹⁸ G. Segato,³⁰ J. E. Seger,⁸⁵ Y. Sekiguchi,¹²⁵ I. Selyuzhenkov,⁹⁶ K. Senosi,⁶⁴ J. Seo,^{66,95} E. Serradilla,^{63,10} A. Sevcenco,⁶¹ A. Shabetai,¹¹² G. Shabratova,⁶⁵ O. Shadura,³ R. Shahoyan,³⁶ A. Shangaraev,¹¹¹ A. Sharma,⁸⁹ N. Sharma,^{60,123} K. Shigaki,⁴⁶ K. Shtejer,^{27,9} Y. Sibiriak,⁹⁹ S. Siddhanta,¹⁰⁵ K. M. Sielewicz,³⁶ T. Siemiarczuk,⁷⁶ D. Silvermyr,^{83,34} C. Silvestre,⁷⁰ G. Simatovic,¹²⁷ R. Singaraju,¹³⁰ R. Singh,^{89,78} S. Singha,^{78,130} V. Singhal,¹³⁰ B. C. Sinha,¹³⁰ T. Sinha,¹⁰⁰ B. Sitar,³⁸ M. Sitta,³² T. B. Skaali,²² K. Skjerdal,¹⁸ M. Slupecki,¹²¹ N. Smirnov,¹³⁴ R. J. M. Snellings,⁵⁶ T. W. Snellman,¹²¹ C. Søgaard,³⁴ R. Soltz,⁷⁴ J. Song,⁹⁵ M. Song,¹³⁵ Z. Song,⁷ F. Soramel,³⁰ S. Sorensen,¹²³ M. Spacek,³⁹ E. Spiriti,⁷¹ I. Sputowska,¹¹⁵ M. Spyropoulou-Stassinaki,⁸⁷ B. K. Srivastava,⁹⁴ J. Stachel,⁹² I. Stan,⁶¹ G. Stefanek,⁷⁶ M. Steinpreis,²⁰ E. Stenlund,³⁴ G. Steyn,⁶⁴ J. H. Stiller,⁹² D. Stocco,¹¹² P. Strmen,³⁸ A. A. P. Suade,¹¹⁸ T. Sugitate,⁴⁶ C. Suire,⁵⁰ M. Suleymanov,¹⁶ R. Sultanov,⁵⁷ M. Šumbera,⁸² T. J. M. Symons,⁷³ A. Szabo,³⁸ A. Szanto de Toledo,¹¹⁸ I. Szarka,³⁸ A. Szczepankiewicz,³⁶ M. Szymanski,¹³¹ J. Takahashi,¹¹⁹ N. Tanaka,¹²⁶ M. A. Tangaro,³³ J. D. Tapia Takaki,^{50,¶} A. Tarantola Peloni,⁵² M. Tariq,¹⁹ M. G. Tarzila,⁷⁷ A. Tauro,³⁶ G. Tejeda Muñoz,² A. Telesca,³⁶ K. Terasaki,¹²⁵ C. Terrevoli,^{25,30} B. Teyssier,¹²⁸ J. Thäder,^{73,96} D. Thomas,^{56,116} R. Tieulent,¹²⁸ A. R. Timmins,¹²⁰ A. Toia,⁵² V. Trubnikov,³ W. H. Trzaska,¹²¹ T. Tsuji,¹²⁵ A. Tumkin,⁹⁸ R. Turrisi,¹⁰⁷ T. S. Tveter,²² K. Ullaland,¹⁸ A. Uras,¹²⁸ G. L. Usai,²⁵ A. Utrobicic,¹²⁷ M. Vajzer,⁸² M. Vala,⁵⁸ L. Valencia Palomo,⁶⁹ S. Vallero,²⁷ J. Van Der Maarel,⁵⁶ J. W. Van Hoorne,³⁶ M. van Leeuwen,⁵⁶ T. Vanat,⁸² P. Vande Vyvre,³⁶ D. Varga,¹³³ A. Vargas,² M. Vargyas,¹²¹ R. Varma,⁴⁷ M. Vasileiou,⁸⁷ A. Vasiliev,⁹⁹ V. Vecchernin,¹²⁹ A. M. Veen,⁵⁶ M. Veldhoen,⁵⁶ A. Velure,¹⁸ M. Venaruzzo,⁷² E. Vercellin,²⁷ S. Vergara Limón,² R. Vernet,⁸ M. Verweij,¹³² L. Vickovic,¹¹⁴ G. Viesti,³⁰ J. Viinikainen,¹²¹ Z. Vilakazi,^{64,124} O. Villalobos Baillie,¹⁰¹ A. Vinogradov,⁹⁹ L. Vinogradov,¹²⁹ Y. Vinogradov,⁹⁸ T. Virgili,³¹ V. Vislavicius,³⁴ Y. P. Viyogi,¹³⁰ A. Vodopyanov,⁶⁵ M. A. Völkl,⁹² K. Voloshin,⁵⁷ S. A. Voloshin,¹³² G. Volpe,³⁶ B. von Haller,³⁶ I. Vorobyev,⁹¹ D. Vranic,^{96,36} J. Vrláková,⁴⁰ B. Vulpescu,⁶⁹ A. Vyushin,⁹⁸ B. Wagner,¹⁸ J. Wagner,⁹⁶ M. Wang,^{7,112} Y. Wang,⁹² D. Watanabe,¹²⁶ M. Weber,^{36,120} S. G. Weber,⁹⁶ J. P. Wessels,⁵³ U. Westerhoff,⁵³ J. Wiechula,³⁵ J. Wikne,²² M. Wilde,⁵³ G. Wilk,⁷⁶ J. Wilkinson,⁹²

M. C. S. Williams,¹⁰⁴ B. Windelband,⁹² M. Winn,⁹² C. G. Yaldo,¹³² Y. Yamaguchi,¹²⁵ H. Yang,⁵⁶ P. Yang,⁷ S. Yano,⁴⁶ S. Yasnopolskiy,⁹⁹ Z. Yin,⁷ H. Yokoyama,¹²⁶ I.-K. Yoo,⁹⁵ I. Yushmanov,⁹⁹ A. Zaborowska,¹³¹ V. Zaccolo,⁷⁹ A. Zaman,¹⁶ C. Zampolli,¹⁰⁴ H. J. C. Zanolli,¹¹⁸ S. Zaporozhets,⁶⁵ A. Zarochentsev,¹²⁹ P. Závada,⁵⁹ N. Zaviyalov,⁹⁸ H. Zbroszczyk,¹³¹ I. S. Zgura,⁶¹ M. Zhalov,⁸⁴ H. Zhang,⁷ X. Zhang,⁷³ Y. Zhang,⁷ C. Zhao,²² N. Zhigareva,⁵⁷ D. Zhou,⁵⁶ Y. Zhou,⁷ Z. Zhou,¹⁸ H. Zhu,⁷ J. Zhu,^{7,112} X. Zhu,⁷ A. Zichichi,^{12,28} A. Zimmermann,⁹² M. B. Zimmermann,^{53,36} G. Zinovjev,³ and M. Zyzak⁴²

(ALICE Collaboration)

¹A.I. Alikhanyan National Science Laboratory (Yerevan Physics Institute) Foundation, Yerevan, Armenia

²Benemérita Universidad Autónoma de Puebla, Puebla, Mexico

³Bogolyubov Institute for Theoretical Physics, Kiev, Ukraine

⁴Bose Institute, Department of Physics and Centre for Astroparticle Physics and Space Science (CAPSS), Kolkata, India

⁵Budker Institute for Nuclear Physics, Novosibirsk, Russia

⁶California Polytechnic State University, San Luis Obispo, California, USA

⁷Central China Normal University, Wuhan, China

⁸Centre de Calcul de l'IN2P3, Villeurbanne, France

⁹Centro de Aplicaciones Tecnológicas y Desarrollo Nuclear (CEADEN), Havana, Cuba

¹⁰Centro de Investigaciones Energéticas Medioambientales y Tecnológicas (CIEMAT), Madrid, Spain

¹¹Centro de Investigación y de Estudios Avanzados (CINVESTAV), Mexico City and Mérida, Mexico

¹²Centro Fermi–Museo Storico della Fisica e Centro Studi e Ricerche “Enrico Fermi,” Rome, Italy

¹³Chicago State University, Chicago, Illinois, USA

¹⁴China Institute of Atomic Energy, Beijing, China

¹⁵Commissariat à l’Energie Atomique, IRFU, Saclay, France

¹⁶COMSATS Institute of Information Technology (CIIT), Islamabad, Pakistan

¹⁷Departamento de Física de Partículas and IGFAE, Universidad de Santiago de Compostela, Santiago de Compostela, Spain

¹⁸Department of Physics and Technology, University of Bergen, Bergen, Norway

¹⁹Department of Physics, Aligarh Muslim University, Aligarh, India

²⁰Department of Physics, Ohio State University, Columbus, Ohio, USA

²¹Department of Physics, Sejong University, Seoul, South Korea

²²Department of Physics, University of Oslo, Oslo, Norway

²³Dipartimento di Elettrotecnica ed Elettronica del Politecnico, Bari, Italy

²⁴Dipartimento di Fisica dell’Università “La Sapienza” and Sezione INFN Rome, Italy

²⁵Dipartimento di Fisica dell’Università and Sezione INFN, Cagliari, Italy

²⁶Dipartimento di Fisica dell’Università and Sezione INFN, Trieste, Italy

²⁷Dipartimento di Fisica dell’Università and Sezione INFN, Turin, Italy

²⁸Dipartimento di Fisica e Astronomia dell’Università and Sezione INFN, Bologna, Italy

²⁹Dipartimento di Fisica e Astronomia dell’Università and Sezione INFN, Catania, Italy

³⁰Dipartimento di Fisica e Astronomia dell’Università and Sezione INFN, Padova, Italy

³¹Dipartimento di Fisica ‘E.R. Caianiello’ dell’Università and Gruppo Collegato INFN, Salerno, Italy

³²Dipartimento di Scienze e Innovazione Tecnologica dell’Università del Piemonte Orientale and Gruppo Collegato INFN, Alessandria, Italy

³³Dipartimento Interateneo di Fisica “M. Merlin” and Sezione INFN, Bari, Italy

³⁴Division of Experimental High Energy Physics, University of Lund, Lund, Sweden

³⁵Eberhard Karls Universität Tübingen, Tübingen, Germany

³⁶European Organization for Nuclear Research (CERN), Geneva, Switzerland

³⁷Faculty of Engineering, Bergen University College, Bergen, Norway

³⁸Faculty of Mathematics, Physics and Informatics, Comenius University, Bratislava, Slovakia

³⁹Faculty of Nuclear Sciences and Physical Engineering, Czech Technical University in Prague, Prague, Czech Republic

⁴⁰Faculty of Science, P.J. Šafárik University, Košice, Slovakia

⁴¹Faculty of Technology, Buskerud and Vestfold University College, Vestfold, Norway

⁴²Frankfurt Institute for Advanced Studies, Johann Wolfgang Goethe-Universität Frankfurt, Frankfurt, Germany

⁴³Gangneung–Wonju National University, Gangneung, South Korea

⁴⁴Gauhati University, Department of Physics, Guwahati, India

⁴⁵Helsinki Institute of Physics (HIP), Helsinki, Finland

⁴⁶Hiroshima University, Hiroshima, Japan

⁴⁷Indian Institute of Technology Bombay (IIT), Mumbai, India

⁴⁸Indian Institute of Technology Indore, Indore (IITI), India

⁴⁹Inha University, Incheon, South Korea

⁵⁰Institut de Physique Nucléaire d’Orsay (IPNO), Université Paris-Sud, CNRS-IN2P3, Orsay, France

⁵¹*Institut für Informatik, Johann Wolfgang Goethe-Universität Frankfurt, Frankfurt, Germany*

⁵²*Institut für Kernphysik, Johann Wolfgang Goethe-Universität Frankfurt, Frankfurt, Germany*

⁵³*Institut für Kernphysik, Westfälische Wilhelms-Universität Münster, Münster, Germany*

⁵⁴*Institut Pluridisciplinaire Hubert Curien (IPHC), Université de Strasbourg, CNRS-IN2P3, Strasbourg, France*

⁵⁵*Institute for Nuclear Research, Academy of Sciences, Moscow, Russia*

⁵⁶*Institute for Subatomic Physics of Utrecht University, Utrecht, Netherlands*

⁵⁷*Institute for Theoretical and Experimental Physics, Moscow, Russia*

⁵⁸*Institute of Experimental Physics, Slovak Academy of Sciences, Košice, Slovakia*

⁵⁹*Institute of Physics, Academy of Sciences of the Czech Republic, Prague, Czech Republic*

⁶⁰*Institute of Physics, Bhubaneswar, India*

⁶¹*Institute of Space Science (ISS), Bucharest, Romania*

⁶²*Instituto de Ciencias Nucleares, Universidad Nacional Autónoma de México, Mexico City, Mexico*

⁶³*Instituto de Física, Universidad Nacional Autónoma de México, Mexico City, Mexico*

⁶⁴*iThemba LABS, National Research Foundation, Somerset West, South Africa*

⁶⁵*Joint Institute for Nuclear Research (JINR), Dubna, Russia*

⁶⁶*Konkuk University, Seoul, South Korea*

⁶⁷*Korea Institute of Science and Technology Information, Daejeon, South Korea*

⁶⁸*KTO Karatay University, Konya, Turkey*

⁶⁹*Laboratoire de Physique Corpusculaire (LPC), Clermont Université, Université Blaise Pascal, CNRS-IN2P3, Clermont-Ferrand, France*

⁷⁰*Laboratoire de Physique Subatomique et de Cosmologie, Université Grenoble-Alpes, CNRS-IN2P3, Grenoble, France*

⁷¹*Laboratori Nazionali di Frascati, INFN, Frascati, Italy*

⁷²*Laboratori Nazionali di Legnaro, INFN, Legnaro, Italy*

⁷³*Lawrence Berkeley National Laboratory, Berkeley, California, USA*

⁷⁴*Lawrence Livermore National Laboratory, Livermore, California, USA*

⁷⁵*Moscow Engineering Physics Institute, Moscow, Russia*

⁷⁶*National Center for Nuclear Studies, Warsaw, Poland*

⁷⁷*National Institute for Physics and Nuclear Engineering, Bucharest, Romania*

⁷⁸*National Institute of Science Education and Research, Bhubaneswar, India*

⁷⁹*Niels Bohr Institute, University of Copenhagen, Copenhagen, Denmark*

⁸⁰*Nikhef, National Institute for Subatomic Physics, Amsterdam, Netherlands*

⁸¹*Nuclear Physics Group, STFC Daresbury Laboratory, Daresbury, United Kingdom*

⁸²*Nuclear Physics Institute, Academy of Sciences of the Czech Republic, Řež u Prahy, Czech Republic*

⁸³*Oak Ridge National Laboratory, Oak Ridge, Tennessee, USA*

⁸⁴*Petersburg Nuclear Physics Institute, Gatchina, Russia*

⁸⁵*Physics Department, Creighton University, Omaha, Nebraska, USA*

⁸⁶*Physics Department, Panjab University, Chandigarh, India*

⁸⁷*Physics Department, University of Athens, Athens, Greece*

⁸⁸*Physics Department, University of Cape Town, Cape Town, South Africa*

⁸⁹*Physics Department, University of Jammu, Jammu, India*

⁹⁰*Physics Department, University of Rajasthan, Jaipur, India*

⁹¹*Physik Department, Technische Universität München, Munich, Germany*

⁹²*Physikalischес Institut, Ruprecht-Karls-Universität Heidelberg, Heidelberg, Germany*

⁹³*Politecnico di Torino, Turin, Italy*

⁹⁴*Purdue University, West Lafayette, Indiana, USA*

⁹⁵*Pusan National University, Pusan, South Korea*

⁹⁶*Research Division and ExtreMe Matter Institute EMMI, GSI Helmholtzzentrum für Schwerionenforschung, Darmstadt, Germany*

⁹⁷*Rudjer Bošković Institute, Zagreb, Croatia*

⁹⁸*Russian Federal Nuclear Center (VNIIEF), Sarov, Russia*

⁹⁹*Russian Research Centre Kurchatov Institute, Moscow, Russia*

¹⁰⁰*Saha Institute of Nuclear Physics, Kolkata, India*

¹⁰¹*School of Physics and Astronomy, University of Birmingham, Birmingham, United Kingdom*

¹⁰²*Sección Física, Departamento de Ciencias, Pontificia Universidad Católica del Perú, Lima, Peru*

¹⁰³*Sezione INFN, Bari, Italy*

¹⁰⁴*Sezione INFN, Bologna, Italy*

¹⁰⁵*Sezione INFN, Cagliari, Italy*

¹⁰⁶*Sezione INFN, Catania, Italy*

¹⁰⁷*Sezione INFN, Padova, Italy*

¹⁰⁸*Sezione INFN, Rome, Italy*

¹⁰⁹*Sezione INFN, Trieste, Italy*

- ¹¹⁰*Sezione INFN, Turin, Italy*
- ¹¹¹*SSC IHEP of NRC Kurchatov Institute, Protvino, Russia*
- ¹¹²*SUBATECH, Ecole des Mines de Nantes, Université de Nantes, CNRS-IN2P3, Nantes, France*
- ¹¹³*Suranaree University of Technology, Nakhon Ratchasima, Thailand*
- ¹¹⁴*Technical University of Split FESB, Split, Croatia*
- ¹¹⁵*The Henryk Niewodniczanski Institute of Nuclear Physics, Polish Academy of Sciences, Cracow, Poland*
- ¹¹⁶*Physics Department, The University of Texas at Austin, Austin, Texas, USA*
- ¹¹⁷*Universidad Autónoma de Sinaloa, Culiacán, Mexico*
- ¹¹⁸*Universidade de São Paulo (USP), São Paulo, Brazil*
- ¹¹⁹*Universidade Estadual de Campinas (UNICAMP), Campinas, Brazil*
- ¹²⁰*University of Houston, Houston, Texas, USA*
- ¹²¹*University of Jyväskylä, Jyväskylä, Finland*
- ¹²²*University of Liverpool, Liverpool, United Kingdom*
- ¹²³*University of Tennessee, Knoxville, Tennessee, USA*
- ¹²⁴*University of the Witwatersrand, Johannesburg, South Africa*
- ¹²⁵*University of Tokyo, Tokyo, Japan*
- ¹²⁶*University of Tsukuba, Tsukuba, Japan*
- ¹²⁷*University of Zagreb, Zagreb, Croatia*
- ¹²⁸*Université de Lyon, Université Lyon 1, CNRS/IN2P3, IPN-Lyon, Villeurbanne, France*
- ¹²⁹*V. Fock Institute for Physics, St. Petersburg State University, St. Petersburg, Russia*
- ¹³⁰*Variable Energy Cyclotron Centre, Kolkata, India*
- ¹³¹*Warsaw University of Technology, Warsaw, Poland*
- ¹³²*Wayne State University, Detroit, Michigan, USA*
- ¹³³*Wigner Research Center for Physics, Hungarian Academy of Sciences, Budapest, Hungary*
- ¹³⁴*Yale University, New Haven, Connecticut, USA*
- ¹³⁵*Yonsei University, Seoul, South Korea*
- ¹³⁶*Zentrum für Technologietransfer und Telekommunikation (ZTT), Fachhochschule Worms, Worms, Germany*

*Deceased.

†Also at M.V. Lomonosov Moscow State University, D.V. Skobeltsyn Institute of Nuclear Physics, Moscow, Russia.

‡Also at University of Belgrade, Faculty of Physics and “Vinča” Institute of Nuclear Sciences, Belgrade, Serbia.

§Permanent address: Konkuk University, Seoul, Korea.

||Also at Institute of Theoretical Physics, University of Wroclaw, Wroclaw, Poland.

¶Also at University of Kansas, Lawrence, Kansas, USA.